


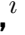











Strong Lensing Tomography: Double and pseudo multi-source plane strong gravitational lensing to constrain dark energy

Paras Sharma^{},^{a,1} Simon Birrer^{},^a Narayan Khadka^{},^{a,b,c} Timo Anguita^{},ⁱ Adam Bolton^{},^c Sydney Erickson^{},^{b,c} Phil Holloway^{},^g Tian Li^{},^d Phil Marshall^{},^{b,c} Dieu D. Nguyen^{},^h Graham P. Smith^{},^j Crescenzo Tortora^{},^f Bryce Wedig^{},^e the Strong Lensing Science Collaboration, and the LSST Dark Energy Science Collaboration

^aDepartment of Physics and Astronomy, Stony Brook University, Stony Brook, NY 11794, USA

^bKavli Institute for Particle Astrophysics and Cosmology, Department of Physics, Stanford University

^cSLAC National Accelerator Laboratory, 2575 Sand Hill Rd., Menlo Park, CA 94025, USA

^dInstitute of Cosmology and Gravitation, University of Portsmouth, Burnaby Rd, Portsmouth PO1 3FX, UK

^eDepartment of Physics and McDonnell Center for the Space Sciences, Washington University, St. Louis, MO 63130, USA

^fINAF – Osservatorio Astronomico di Capodimonte, Salita Moiariello 16, I-80131, Napoli, Italy

^gDepartment of Physics, Oxford University, Keble Road, Oxford, OX1 3RH, UK

^hUniversity of Michigan, 500 S State St, Ann Arbor, MI 48109, USA

ⁱInstituto de Astrofísica, Departamento de Física y Astronomía, Facultad de Ciencias Exactas, Universidad Andres Bello, Fernández Concha 700, Santiago, Chile

^jSchool of Physics and Astronomy, University of Birmingham, Birmingham, B15 2TT, United Kingdom

¹Corresponding author.

E-mail: paras.sharma@stonybrook.edu, simon.birrer@stonybrook.edu

Abstract. Tomographic measurements of gravitational lensing with different lens and source redshift distributions contain crucial information about the universe’s relative expansion rate, and hence dark energy. While this technique is well-established in weak lensing, its application to strong lensing has traditionally focused on Double Source Plane Lenses (DSPLs). However, DSPLs are exceedingly rare and fundamentally limited by the Mass-Sheet Degeneracy (MSD), a systematic uncertainty underexplored in previous literature. To overcome these challenges, we introduce Pseudo Double-Source Plane Lenses (PDSPLs): pairs of independent single-source plane lenses with self-similar deflectors. This generalizes the DSPL formalism to the $\sim 10^5$ galaxy-galaxy lenses expected from upcoming surveys like LSST, Euclid, and Roman. Unlike true DSPLs, PDSPLs are free from the intermediate source mass problem by construction, eliminating the associated secondary MSD and the need for multi-plane ray tracing. We incorporate the deflector galaxy’s MSD into a hierarchical forecasting framework, demonstrating that this degeneracy severely degrades constraints from small DSPL samples, thus motivating our PDSPL statistical approach. We forecast constraints on the dark energy equation of state under a Flat w_0w_a CDM cosmology. The LSST 10-year photometric sample alone achieves $\sigma(w_0) \sim 0.45$, while simultaneously constraining the MSD parameter and deflector power-law slope to $\sim 2\%$. Adding a prior $\mathcal{N}(0.3, 0.05)$ on Ω_m — simulating combination with external probes like CMB, BAO, or SNe Ia — tightens this to $\sigma(w_0) \sim 0.29$, competitive with current Stage III weak lensing analyses. Notably, this massive photometric sample outperforms smaller subsets with precise spectroscopic follow-up (e.g., from 4MOST), confirming statistical volume dominates over per-pair precision.

Contents

1	Introduction	2
2	Multi-source plane lensing formalism	3
2.1	Single plane lensing	3
2.2	Double source plane lensing	3
3	Mass-sheet degeneracy and multi-source-plane lensing	4
3.1	The MST with a single lens and source plane	4
3.2	The MST with two source planes	5
3.3	The MST in DSP with a power-law density profile	5
4	Generalized pseudo-multi-source plane lensing	6
4.1	Pseudo Double Source Plane Lenses	7
4.2	Noise in interpreting PDSPL as DSPL	7
4.3	Deflector Self-Similarity	9
4.4	Photometric vs Spectroscopic Observables for Pairing Deflector Galaxies	9
4.5	Elliptical Galaxies and the Lensing Mass Fundamental Plane (MFP)	10
4.6	Simulated galaxy-galaxy lenses from SLSim	11
4.7	Finding Self-Similar Deflector Pairs within SLSim lenses	12
5	Forecasts for DSPL and PDSPL with MST	17
5.1	Analytical error propagation	17
5.2	Likelihood Function	18
5.3	Simulated PDSPLs and DSPLs for forecasting	20
5.4	Numerical forecast with hierarchical inference	20
6	Discussion	22
6.1	Geometric Simplicity and Avoiding Intermediate Source MST	22
6.2	Observational Yield and Survey Constraints	24
6.3	Optimizing Deflector Pairing	26
6.4	Self-Calibration of $\sigma_{\beta_E, \mathcal{D}}$	27
6.5	Synergy with External Datasets	28
6.6	Systematic Uncertainties	28
6.7	Comparison with Literature and the Impact of Degeneracies	28
7	Conclusion	29
A	Numerical compression and Asimov forecasting	38
B	The Impact of Spectroscopic Redshifts on PDSPL Cosmology	38
C	Inferring Dissimilarity Scatter $\sigma_{\beta_E, \mathcal{D}}$	39

1 Introduction

Understanding the fundamental nature of dark energy remains one of the most pressing challenges in modern cosmology. Recent observations—including evidence for potential dynamical dark energy [1–3], along with persistent tensions with Λ CDM [4, 5]—have intensified interest in exploring dark energy physics beyond the standard cosmological constant [6–10]. These developments motivate the search for robust, late-time geometric probes. Tomographic measurements of gravitational lensing—which track how the deflection of light evolves across sources at varying distances—provides a powerful, purely geometric probe of the Universe’s expansion history and the dark energy equation of state. By analysing the relative deflection of light from sources at varying distances, we can constrain these cosmological parameters and break the degeneracies often inherent to single-plane measurements [11, 12].

This tomographic approach has been prominently applied to weak lensing shape measurements with multiple redshift bins in the lens and source population [13]. In the strong lensing regime, the technique relies on the rare alignment of multiple sources behind a single deflector. Galaxy clusters, acting as dominant deflectors for multiple background sources at distinct redshifts, have proven to be powerful laboratories for this method [14, 15]. While the alignment of two distinct sources behind a single galaxy-scale deflector—forming a double-source plane lens (DSPL)—is exceptionally rare, these systems offer unique value. When identified, the ratio of their Einstein radii yields a robust cosmological observable independent of the Hubble constant (H_0) that has been successfully used to constrain the dark energy equation of state [16–20].

Despite their conceptual appeal, DSPLs remain exceedingly rare, with only a small number of confirmed systems to date [e.g., 16, 21–25]. Moreover, DSPLs present unique modeling challenges; standard analyses often neglect the "compound lensing" effect—where the intermediate source acts as a secondary deflector—an approximation that degrades when the sources are widely separated in redshift [18]. These limitations motivate the search for alternative strategies that retain the geometric sensitivity of DSPLs while mitigating their observational sparsity and modelling complexity.

We are currently entering the era of next-generation wide-field surveys. Facilities such as the Vera C. Rubin Observatory, which will conduct the Legacy Survey of Space and Time [LSST; 26], Euclid [27], and the Nancy G. Roman Space Telescope [formerly WFIRST; 28] are expected to discover $\mathcal{O}(10^5)$ galaxy-scale strong lenses [29–32]. This dramatic increase in sample size opens new avenues for extracting cosmological signals from the population statistics of strong lenses, rather than relying on rare individual alignments.

To capitalize on these upcoming catalogs, we propose *pseudo* double-source plane lenses (PDSPLs): pairs of independent strong lenses, each with its own deflector and source, selected such that the deflectors are approximately self-similar. With these considerations, the systems can be treated as an approximate DSPL, enabling the extraction of a generalized Einstein radius ratio observable. This approach effectively transforms strong lensing tomography from a search for rare alignments into a statistics-driven science, capitalizing on the vast catalogs of single-source plane lenses anticipated from upcoming surveys [29, 30]. Crucially, this method does not rely on expensive velocity dispersion measurements and possesses systematic uncertainties distinct from those of weak lensing tomography.

The cosmological constraining power of DSPL and PDSPL Einstein radius ratio are fundamentally limited by uncertainties in the deflector’s mass profile. This is primarily due to the well-known mass-sheet degeneracy [MSD; 33], which allows for transformations of

the lensing mass distribution that preserve image positions but alter inferred mass scales. As demonstrated by [34], this degeneracy limits the precision with which one can extract cosmological information from DSPLs unless it is explicitly broken by external datasets (e.g. stellar kinematics) or statistically constrained [35, 36].

In this paper, we derive how the observables in (P)DSPL transform under an MSD and what quantities remain invariant. We perform a detailed updated hierarchical forecast on the dark energy equation of state parameters using DSPL treating the uncertainty in the MSD as a covariant error on the population level.

Further, to assess the cosmological utility of PDSPLs, we generate a realistic, population-level simulation of galaxy-galaxy lenses expected to be observed by LSST, pair near-identical deflectors, and perform a hierarchical forecast to constrain dark energy equation of state parameters. We further project the capabilities of upcoming surveys in leveraging either PDSPLs or DSPLs for precision cosmology.

This paper is structured as follows: In Section 2 we provide the basic formalism for single- and double-source plane lensing. Section 3 details the formalism of the mass-sheet degeneracy in both single- and double-source plane lensing. Specifically, we derive how the observable ratio of two Einstein radii transforms under an MSD for a power-law deflector mass density. In Section 4, we generalize the DSPL method to near-identical pairs of lenses with different sources and derive the criteria under which two single-source plane lenses can be combined into an approximate double-source plane lens. In Section 5 we provide a forecast for the expected constraints on the dark energy equation of state from the expected set of DSPLs and PDSPLs that LSST can provide. We provide further discussions of the newly proposed method in Section 6 and conclude in Section 7.

2 Multi-source plane lensing formalism

2.1 Single plane lensing

In general, we denote $\boldsymbol{\beta}$ as the unlensed angular coordinate of the source, $\boldsymbol{\theta}$ as the observed angular coordinate of the lensed image on the sky, and $\boldsymbol{\alpha}$ as the reduced angular deflection vector mapping the two. The lens equation (Equation 2.1) describes this geometric distortion:

$$\boldsymbol{\beta} = \boldsymbol{\theta} - \boldsymbol{\alpha}(\boldsymbol{\theta}). \quad (2.1)$$

In case of a single deflector, the physical deflection angle $\hat{\boldsymbol{\alpha}}$ is related to the reduced deflection angle $\boldsymbol{\alpha}$ as

$$\boldsymbol{\alpha}(\boldsymbol{\theta}) = \frac{D_{\text{ds}}}{D_{\text{s}}} \hat{\boldsymbol{\alpha}}(D_{\text{d}}\boldsymbol{\theta}), \quad (2.2)$$

where D_{s} is the angular diameter distance from the observer to the source, and D_{ds} is the angular diameter distance from the deflector to the source, respectively.

2.2 Double source plane lensing

For a single deflector at redshift z_{d} lensing two background sources at redshifts z_{s1} and z_{s2} , measuring the resulting Einstein radii $\theta_{\text{E},1}$ and $\theta_{\text{E},2}$ yields a distance ratio constraint.

For two photons passing through the same point in the lens plane, but originating on different source planes, the ratio of scaled deflection angles is

$$\frac{\alpha_1}{\alpha_2} = \frac{D_{\text{ds}1}D_{\text{s}2}}{D_{\text{ds}2}D_{\text{s}1}} \equiv \beta, \quad (2.3)$$

where D_{si} is the angular diameter distance from the observer to the i 'th source, and $D_{\text{ds}i}$ is the angular diameter distance to the i 'th source when observed from the deflector.

For Einstein radii that are not formed at the same angular position, the interpretation of the comparison between two or more Einstein radii becomes model dependent. The primary cosmology-relevant observable in a DSPL is the ratio of Einstein radii

$$\beta_{\text{E}} \equiv \frac{\theta_{\text{E},1}}{\theta_{\text{E},2}}. \quad (2.4)$$

For a singular isothermal sphere (SIS) deflector, the deflection angle is constant as a function of radius, i.e.

$$\alpha_{\text{SIS}}(\theta) = \theta_{\text{E}}, \quad (2.5)$$

hence, the ratio of Einstein radii, β_{E} is identical to the quantity β in Equation 2.3, $\beta_{\text{E,SIS}} = \beta$.

The deflection angle of a power-law mass density with logarithmic three-dimensional density profile slope γ_{pl} is

$$\alpha_{\text{PL}}(\theta) = \theta_{\text{E}} \left(\frac{\theta}{\theta_{\text{E}}} \right)^{(2-\gamma_{\text{pl}})}. \quad (2.6)$$

Given two Einstein radii measurements, we can calculate the ratio of deflection angles at any point, such as at the angle of the two Einstein radii, which is given by

$$\beta = \frac{\alpha_{\text{pl},1}(\theta_{\text{E},1})}{\alpha_{\text{pl},2}(\theta_{\text{E},1})} = \frac{\alpha_{\text{pl},1}(\theta_{\text{E},2})}{\alpha_{\text{pl},2}(\theta_{\text{E},2})} = (\beta_{\text{E,pl}})^{\gamma_{\text{pl}}-1}. \quad (2.7)$$

We recover the expression of β for a SIS profile (Eqn. 2.5) with the isothermal power-law slope $\gamma_{\text{pl}} = 2$.

3 Mass-sheet degeneracy and multi-source-plane lensing

3.1 The MST with a single lens and source plane

The mass-sheet transform (MST) is a multiplicative transform of the lens equation preserving image positions (and thus any higher order differentials too) under a linear source displacement $\boldsymbol{\beta} \rightarrow \lambda\boldsymbol{\beta}$ and was introduced by [33, 37] as such

$$\lambda_{\text{MST}}\boldsymbol{\beta} = \boldsymbol{\theta} - \lambda_{\text{MST}}\boldsymbol{\alpha}(\boldsymbol{\theta}) - (1 - \lambda_{\text{MST}})\boldsymbol{\theta}. \quad (3.1)$$

The term $(1 - \lambda_{\text{MST}})\boldsymbol{\theta}$ in Equation 3.1 describes an infinite sheet of convergence, κ (defined as the dimensionless surface mass density), hence the name Mass-Sheet Transform (MST). The MST is the mathematical transformation that gives rise to the Mass-Sheet Degeneracy (MSD). Thus, the corresponding transform of the convergence profile is given by

$$\kappa_{\text{MST}}(\boldsymbol{\theta}) = \lambda_{\text{MST}}\kappa(\boldsymbol{\theta}) + (1 - \lambda_{\text{MST}}). \quad (3.2)$$

The MST can be described as a global transform of the convergence and hence it can lead to physical solutions for a wide range of values of λ_{MST} . A fact that makes the MST a prominent and relevant degeneracy for many applications, in particular the measurement of

the Hubble constant with time-delay cosmography [38–41]. Only observables related to the absolute source size, intrinsic magnification of the lensed source, the absolute lensing potential, or the relative time delay when imposing a known cosmology with absolute distances, are able to break this degeneracy.

3.2 The MST with two source planes

The strict mathematical form of the MST is broken when introducing two or more source planes. Let us perform an MST to a first source plane, z_{s1} , with corresponding $\lambda_{\text{MST},1}$ (Eqn. 3.1). The physical deflection angle at the deflector plane is then (Eqn. 2.2)

$$\hat{\alpha}_{\lambda_1}(\boldsymbol{\theta}) = \lambda_1 \frac{D_{s1}}{D_{\text{ds1}}} \boldsymbol{\alpha}_1(\boldsymbol{\theta}) + (1 - \lambda_1) \frac{D_{s1}}{D_{\text{ds1}}} \boldsymbol{\theta}, \quad (3.3)$$

where we referred to $\boldsymbol{\alpha}_1$ as the reduced deflection field to z_{s1} prior to an MST. When evaluating the reduced deflection field for the second source plane z_{s2} , the reduced deflection field results in

$$\boldsymbol{\alpha}_{2,\lambda_1}(\boldsymbol{\theta}) = \lambda_1 \frac{D_{s1} D_{\text{ds2}}}{D_{\text{ds1}} D_{s2}} \boldsymbol{\alpha}_1(\boldsymbol{\theta}) + (1 - \lambda_1) \frac{D_{s1} D_{\text{ds2}}}{D_{\text{ds1}} D_{s2}} \boldsymbol{\theta}. \quad (3.4)$$

We can now substitute the relative apparent deflection scaling β (Eqn. 2.3) in the equation above, and convert the apparent deflection field $\boldsymbol{\alpha}_2 = \boldsymbol{\alpha}_1/\beta$

$$\boldsymbol{\alpha}_{2,\lambda_1}(\boldsymbol{\theta}) = \lambda_1 \boldsymbol{\alpha}_2(\boldsymbol{\theta}) + (1 - \lambda_1) \frac{1}{\beta} \boldsymbol{\theta}. \quad (3.5)$$

The equation above is not an invariant MST anymore. Re-writing the equation above to the closest form of the MST is

$$\boldsymbol{\alpha}_{2,\lambda_1}(\boldsymbol{\theta}) = \lambda_1 \boldsymbol{\alpha}_2(\boldsymbol{\theta}) + (1 - \lambda_1) \boldsymbol{\theta} + \left(\frac{1}{\beta} - 1 \right) (1 - \lambda_1) \boldsymbol{\theta}. \quad (3.6)$$

In short, an MST for one source plane, z_{s1} , with λ_1 , leads to a transform at a different source plane, z_{s2} that is the combination of an MST with the same λ with an additional convergence term $(\beta^{-1} - 1)(1 - \lambda)$. Consequently, the second source experiences a modified deflection field that physically alters its corresponding Einstein radius—a measurable shift that we quantify in the following section.

3.3 The MST in DSP with a power-law density profile

There exists no general relation between a sheet of mass/convergence and the change of the Einstein radius, as it depends on the radial projected mass density profile of the deflector. For a power-law density profile (Eqn. 2.6), a mass sheet with convergence κ_{mst} changes the Einstein radius by ¹

$$\theta_{\text{E,pl}+\kappa} = \theta_{\text{E,pl}} (1 - \kappa)^{\frac{1}{1-\gamma_{\text{pl}}}}. \quad (3.7)$$

For a power-law density profile that is invariantly transformed under an MST at the source plane z_{s1} with λ_1 (meaning, among other lensing observables, that θ_{E1} remains unchanged), this transformation will change the Einstein radius at the second source plane z_{s2} , θ_{E2} , as (Eqns. 3.6+3.7):

¹The new Einstein radius is defined demanding $\alpha_{\text{pl}+\kappa}(\theta_{\text{E,pl}+\kappa}) = \theta_{\text{E,pl}+\kappa}$.

$$\left(\frac{\theta_{\text{E1}}}{\theta_{\text{E2}}}\right)_\lambda = \left(\frac{\theta_{\text{E1}}}{\theta_{\text{E2}}}\right)_{\lambda=1} \left(1 - (1 - \lambda) \left(\frac{1}{\beta} - 1\right)\right)^{\frac{1}{\gamma_{\text{pl}}-1}}. \quad (3.8)$$

Putting it all together, combining the result of the MST of the equation above (Eqn. 3.8) with the scaling of the power-law slope excluding the MST (Eqn. 2.7), the ratio of two Einstein radii θ_{E1} and θ_{E2} for two source redshifts z_{s1} and z_{s2} scales with power-law slope γ_{pl} and mass-sheet term λ as

$$\beta_{\text{E,pl}} = \left(\frac{\theta_{\text{E1}}}{\theta_{\text{E2}}}\right)_{\lambda, \gamma_{\text{pl}}} = \beta^{\frac{1}{\gamma_{\text{pl}}-1}} \left(1 - (1 - \lambda) \left(\frac{1}{\beta} - 1\right)\right)^{\frac{1}{1-\gamma_{\text{pl}}}} = (\beta - (1 - \lambda)(1 - \beta))^{\frac{1}{\gamma_{\text{pl}}-1}}. \quad (3.9)$$

The observable, the ratio of two Einstein radii, is hence a function of not only the cosmology (encompassed in β), but also of the MST parameter λ and the power-law density slope γ_{pl} . Solving Equation 3.9 for β results in

$$\beta = \frac{1}{2 - \lambda} \left[\left(\frac{\theta_{\text{E1}}}{\theta_{\text{E2}}}\right)^{\gamma_{\text{pl}}-1} + (1 - \lambda) \right]. \quad (3.10)$$

It is important to note that the above formalism represents an *idealized* Double Source Plane Lens (DSPL) scenario, where the intermediate source (at z_{s1}) is treated purely as a luminous background object and its own mass is neglected. In true, physical DSPL systems, the intermediate source acts as a secondary deflector, introducing a complex compound lensing effect and a secondary, independent mass-sheet degeneracy associated with the first source plane [18]. By neglecting this intermediate mass, we isolate the fundamental geometric distance scaling and any associated MST-like degrees of freedom. Crucially, this idealized, mathematically simpler configuration is exactly the regime that our Pseudo-DSPL (PDSPL) framework emulates (Section 4).

4 Generalized pseudo-multi-source plane lensing

A *Pseudo Multi-Source Plane Lens* (PMSPL) may be constructed by pairing multiple single-source plane lens systems, under the assumption that the deflectors exhibit sufficiently similar mass distributions. The primary motivation for this approach stems from the observational reality: while genuine double- or multi-source plane lenses (DSPLs or MSPLs) are intrinsically rare and challenging to identify in current datasets, the number of confirmed single-source plane lenses is already substantial and poised to increase dramatically. Next-generation wide-field surveys are expected to uncover $\sim \mathcal{O}(10^5)$ strong lensing systems [30], greatly enhancing the likelihood of identifying deflector pairs with near-identical properties.

A key consideration in this framework is quantifying the required degree of similarity between deflectors for the PMSPL approximation to remain valid. Equally important is the practical challenge of identifying such near-identical systems within large, structurally diverse datasets. These two aspects—theoretical tolerance and observational identifiability—represent distinct but related challenges. In both cases, one can define a characteristic noise floor that captures the uncertainty introduced by residual differences between deflectors.

Despite these challenges, the observational advantage of this approach is clear. The ability to form PMSPLs from the vastly more numerous population of single-source plane lenses opens the door to tomographic cosmological analyses at a scale that would be infeasible

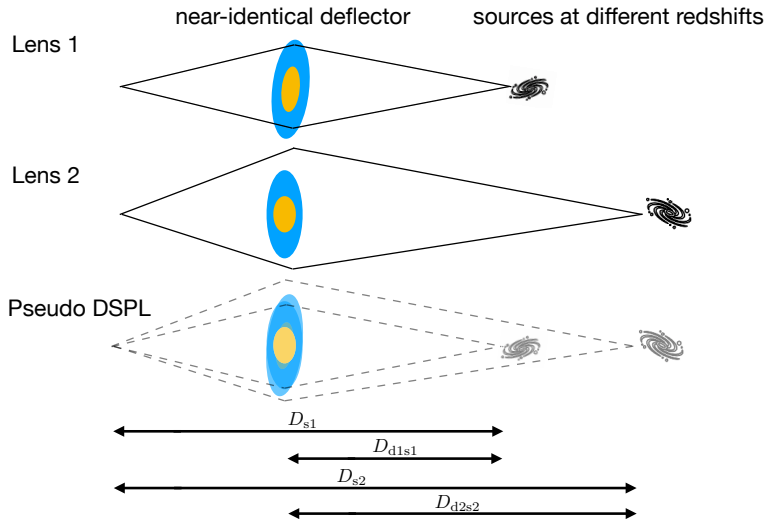


Figure 1. Illustration of two separate lenses with near-identical deflectors and sources at different redshifts. Near-identical pairs of deflectors can be used as pseudo double source plane lenses.

relying solely on genuine DSPL or MSPL systems, which are expected to remain sparse even in future surveys.

4.1 Pseudo Double Source Plane Lenses

A pseudo double-source plane lens (PDSPL) represents the simplest realization of the broader PMSPL framework, constructed from a pair of single-source plane lenses whose deflectors exhibit near-identical mass profiles. An illustrative example of such a configuration is shown in Figure 1. Importantly, the mathematical formalism developed for conventional double-source plane lenses (DSPLs) remains directly applicable to PDSPLs, provided the pair of lenses possess self-similar deflectors. In what follows, we focus exclusively on the PDSPL case, which captures the essential features of the approach while offering a tractable starting point for both analytical development and observational implementation.

4.2 Noise in interpreting PDSPL as DSPL

In the context of this paper, self-similarity of deflectors is closely tied to whether a pair of single-source plane lenses can mimic a DSPL. To answer this question, we refer to Figure 1. Assuming the first lens system has a deflector at z_{D1} and the source at z_{S1} , and the second lens system has a deflector at z_{D2} and the source at z_{S2} . The observable quantity relevant for PDSPL analysis is

$$\beta_{E,\text{pseudo}} \equiv \frac{\theta_{E,D1,S1}}{\theta_{E,D2,S2}} \quad (4.1)$$

where θ_{E,D_i,S_j} is the Einstein radii for the lens configuration with deflector D_i and source S_j . Note that in practice, $i = j$ corresponds to the observed single-source plane lenses where we directly measure $\theta_{E,D1,S1}$ and $\theta_{E,D2,S2}$ from observed images.

Now, imagine if we place the source $S2$ behind deflector $D1$ such that $z_{D1} < z_{S1} < z_{S2}$ (see Figure 2) then there will be a different Einstein radii from the source $S2$ and the ratio of

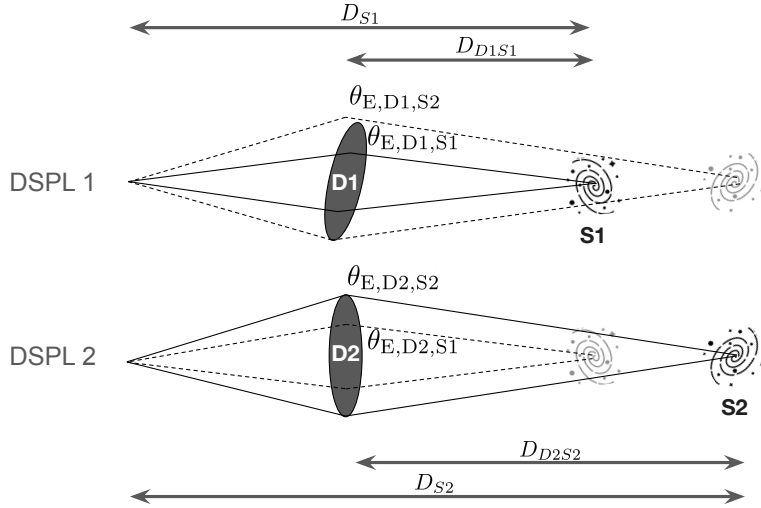


Figure 2. Illustration of the two possible DSPL configurations obtained by placing one source behind the deflector of the other lensing system. In the “DSPL 1” configuration, a virtual source S2 is positioned behind deflector D1 in addition to the existing source S1. Conversely, in the “DSPL 2” configuration, a virtual source S1 is placed behind deflector D2 along with the existing source S2. The corresponding Einstein radii for each configuration are indicated in the figure.

Einstein radii from a true DSPL configuration (with deflector D1) will be

$$\beta_{E,DSPL,D1} \equiv \frac{\theta_{E,D1,S1}}{\theta_{E,D1,S2}} \quad (4.2)$$

Similarly if we place source S1 behind behind deflector D2 such that $z_{D2} < z_{S1} < z_{S2}$ then there will be a different Einstein radii from the source S1 and the ratio of Einstein radii from a true DSPL configuration (with deflector D2) will be

$$\beta_{E,DSPL,D2} \equiv \frac{\theta_{E,D2,S1}}{\theta_{E,D2,S2}} \quad (4.3)$$

Thus, we define $\beta_{E,DSPL} = \text{mean}(\beta_{E,DSPL,D1}, \beta_{E,DSPL,D2})$ and the relative scatter in $\beta_{E,pseudo}$ that is expected in interpreting a PDSPL as an approximate DSPL

$$\frac{\Delta\beta_E}{\beta_E} = \frac{\beta_{E,pseudo} - \beta_{E,DSPL}}{\beta_{E,DSPL}}. \quad (4.4)$$

For near-identical deflectors, this must be very small and one main goal of the paper is to characterize how small this error can get. Note that this is different from the observed error on $\beta_{E,pseudo}$, which is obtained from observed error on Einstein radii. For a population of paired lens systems, one can obtain the relative scatter using the standard deviation, where

$$\frac{\Delta\beta_E}{\beta_E} \Big|_{\text{pop.}} = \text{std} \left(\frac{\beta_{E,pseudo} - \beta_{E,DSPL}}{\beta_{E,DSPL}} \right) \quad (4.5)$$

This relative scatter in β_E arises from subtle variations in the physical properties of the paired deflectors. Ideally, identifying near-identical deflectors in observed systems would involve minimizing $\Delta\beta_E/\beta_E$; however, this quantity is not directly observable. Consequently, in the following subsection, we define a deflector pair dissimilarity parameter as an observational proxy that correlates directly with the relative scatter in β_E .

4.3 Deflector Self-Similarity

In order for a pair of single-source plane lenses to be considered a PDSPL (or an approximate DSPL) we need to determine the criterion for two deflectors to be near-identical (or self-similar). Assuming deflectors to be elliptical galaxies, a non-exhaustive list of deflector properties to describe them can be: their redshift (z_D), velocity dispersion ($\sigma_{v,D}$), effective radius (R_e), observed magnitudes or fluxes ($m_{X,D}$ or $f_{X,D}$), ellipticity (ε_D), average surface brightness (μ_e) within R_e , or their lensing mass surface density ($\Sigma_{1/2}$), defined as the mean projected surface mass density within $R_e/2$ (as per the convention in [42, 43]).

The relative differences ($\Delta z_D/z_D$, $\Delta\sigma_{v,D}/\sigma_{v,D}$, \dots) in these parameters between the two deflectors sets the criteria of self-similarity. Here we define these quantities as

$$\frac{\Delta z_D}{z_D} \equiv \frac{|z_{D1} - z_{D2}|}{\text{mean}(z_{D1}, z_{D2})} ; \quad \frac{\Delta\sigma_{v,D}}{\sigma_{v,D}} \equiv \frac{|\sigma_{v,D1} - \sigma_{v,D2}|}{\text{mean}(\sigma_{v,D1}, \sigma_{v,D2})} ; \quad \dots \quad (4.6)$$

For a population of deflector pairs indexed with i , the relative scatter can be defined as

$$\left. \frac{\Delta z_D}{z_D} \right|_{\text{pop.}} \equiv \text{std} \left(\frac{\Delta z_{Di}}{z_{Di}} \right) ; \quad \left. \frac{\Delta\sigma_{v,D}}{\sigma_{v,D}} \right|_{\text{pop.}} \equiv \text{std} \left(\frac{\Delta\sigma_{v,Di}}{\sigma_{v,Di}} \right) ; \quad \dots \quad (4.7)$$

where Δz_{Di} represents the redshift difference and z_{Di} represents the mean redshift for the two deflectors in i 'th pair. The same convention is followed for $\sigma_{v,D}$ and other deflector properties as well.

To quantify how similar or dissimilar deflectors can get, we define the deflector pair dissimilarity parameter for the i 'th deflector pair as

$$\mathcal{D}_i(z_D, R_e, \dots) = \sqrt{\frac{1}{N_{\text{pp}}} \left(\left| \frac{\Delta z_{Di}}{z_{Di}} \right|^2 + \left| \frac{\Delta R_{ei}}{R_{ei}} \right|^2 + \dots \right)}. \quad (4.8)$$

which depends on the parameters used for pairing the deflectors and N_{pp} specifies the total number of these ‘‘pairing parameters’’. A smaller value of $\mathcal{D}_i(z_D, R_e, \dots)$ indicates near-identical deflectors. We note that while a fractional difference (e.g., $\Delta X/X$) is physically meaningful for linear quantities, computing it for logarithmic quantities like magnitudes (m_i) and colors is physically unorthodox due to arbitrary zero-points. Thus we convert magnitudes to fluxes and colors to flux ratios and use them as pairing parameters. While this unweighted Euclidean metric provides a functional baseline for identifying pairs in our simulated forecasts, the observational parameters do not impact the lensing observables equally. A weighted distance metric is a natural and necessary extension for real survey data. We discuss this optimization further in Section 6.3.

4.4 Photometric vs Spectroscopic Observables for Pairing Deflector Galaxies

Upcoming wide-field imaging surveys, including LSST, Euclid, and Roman, will provide a wealth of photometric data for an unprecedented number of deflector galaxies, yielding an estimated sample of $\sim 120,000$ galaxy-scale strong lenses (predominantly massive elliptical deflectors) [29–32] from LSST alone. For each system, these surveys will deliver multi-band photometric magnitudes, morphological parameters derived from the galaxy’s light profile (e.g., effective radius), and photometric redshifts with a target precision of $\sigma_z/(1+z) < 0.05$ [44].

Complementary spectroscopic follow-up campaigns with facilities like the 4-metre Multi-Object Spectroscopic Telescope (4MOST) are projected to secure precise spectroscopic redshifts for a subset of $\sim 10,000$ of these galaxy-galaxy lenses [45]. Furthermore, these observations will yield central stellar velocity dispersion (σ_v) measurements—a key dynamical probe—for approximately 5,000 of these deflector galaxies.

This significant disparity in sample sizes between the photometric and spectroscopic datasets motivates our investigation. The vast majority of deflector galaxies will have well-measured photometric properties but will lack direct spectroscopic redshift and velocity dispersion measurements. Therefore, it is essential to determine if these purely photometric data are sufficient for identifying near-identical deflectors. The physical basis for this approach lies in the well-established scaling relations that massive elliptical galaxies obey, such as the Fundamental Plane [46, 47]. This self-regularity connecting dynamical properties (like $\sigma_{v,D}$) to photometric observables (like effective radius and surface brightness or the surface mass density) suggests that deflectors can indeed be paired photometrically, with a precision limited by the intrinsic scatter in these scaling relations.

4.5 Elliptical Galaxies and the Lensing Mass Fundamental Plane (MFP)

The population-level scatter in the physical properties of deflector galaxies directly influences the pairing quantities described in Equation 4.7. Characterizing this scatter requires an understanding of the structural and dynamical regularities exhibited by massive elliptical galaxies.

Elliptical galaxies obey a range of empirical scaling relations that link their photometric, structural, and dynamical properties, evidencing their self-regularity. Key examples include the Faber–Jackson relation between luminosity and stellar velocity dispersion [48], the Kormendy relation between surface brightness and effective radius [49], and the fundamental plane (FP) combining R_e , I_e , and $\sigma_{v,D}$ into a thin manifold [46, 47]. Additional trends, such as the color–magnitude relation [50], mass–metallicity relation [51], and $M_{\text{BH}}\text{--}\sigma$ relation [52, 53], further indicate that massive ellipticals evolve under self-regulating processes that drive them toward common equilibrium configurations.

In the context of gravitational lensing, a more physically motivated extension of the FP is the *lensing mass–fundamental plane* (MFP; [42, 43, 54]), in which surface brightness I_e is replaced by the mean projected surface mass density $\Sigma_{1/2}$, defined within $R_e/2$ following [42, 43]. The existence of the FP and MFP implies that, to within a small scatter, $\sigma_{v,D}$ can be estimated from R_e and either I_e or $\Sigma_{1/2}$, allowing key deflector parameters to be inferred from accessible observables.

Previous studies [42, 43] have analyzed the SLACS, SL2S, and TDCOSMO lens samples to study their MFP. Both studies [42, 43] found that the lenses are distributed around the MFP with very small intrinsic scatter of \sim a few percent. This scatter is notably reduced compared to the intrinsic scatter of the traditional FP [55], implying more regularity in properties of elliptical galaxies. Crucially, this structural regularity is most pronounced at the high-mass end; the brightest, most massive elliptical galaxies reside at the tightest end of these scaling relations [56]. Consequently, predicting the underlying mass profile of a highly luminous deflector from its photometric properties is inherently less noisy than doing so for lower-mass systems. Thus, the inclusion of $\Sigma_{1/2}$ and $R_e/2$ in addition to z_D could offer an optimal strategy for finding near-identical deflectors. However, in observations, estimating $\Sigma_{1/2}$ from measured Einstein radius, is not cosmological model independent [see Equation

14 and 15 in 43]. Consequently, employing $\Sigma_{1/2}$ to pair deflectors and subsequently infer cosmological parameters may introduce a systematic bias into the analysis.

Nevertheless, the existence of the MFP provides a crucial physical insight: elliptical galaxies exhibit a higher degree of structural regularity than that suggested by traditional FP. The wealth of incoming data with upcoming surveys may offer avenues to further explore these narrower scaling relations in future. However, prioritizing cosmological model independence is paramount for the current analysis. Therefore, we seek a matching strategy that capitalizes on this intrinsic regularity but restricts itself to observables that do not introduce circularity.

To mitigate potential biases arising from the cosmology-dependent estimation of $\Sigma_{1/2}$, we explore a matching strategy based exclusively on the direct observed photometric properties of the deflectors. Specifically, we investigate pairings constructed using the lens redshift (z_D), effective radius (R_e), apparent magnitude in multiple bands ($m_{X,D}$), and colors ($m_{X,D} - m_{Y,D}$). In subsequent sections we show that these photometric observables alone can effectively identify near-identical deflectors to a reasonable precision without invoking any cosmological dependence. Further we also show the effectiveness of matching deflector pairs with spectroscopically measured deflector redshift and velocity dispersion.

4.6 Simulated galaxy-galaxy lenses from SLSim

To investigate how the scatter in the properties of paired deflectors propagates to the observed scatter in $\beta_{E,\text{pseudo}}$, we simulate single-source-plane (galaxy-galaxy) lenses using the SLSim (Strong-Lensing Simulation)² pipeline [57]. The simulations are performed assuming a Flat- Λ CDM cosmology with $H_0 = 70 \text{ km s}^{-1} \text{ Mpc}^{-1}$, $\Omega_m = 0.3$, and $w = -1$.

The deflector population is modelled as elliptical (red) galaxies with a power-law mass density profile having $\langle \gamma_{\text{pl}} \rangle = 2.078$ with an intrinsic scatter of $\sigma(\gamma_{\text{pl}}) = 0.16$ [42], spanning a redshift range of $z_D \in [0.01, 2.5]$. The background sources are modelled as spiral (blue) galaxies with redshifts $z_S \in [0.1, 5.0]$. In SLSim elliptical galaxies are modelled using a double Schechter function [58] using the `skypy` [59] pipeline to encompass both massive and dwarf populations. The velocity dispersions for these galaxies are drawn by abundance matching with the observed SDSS velocity dispersion distribution [60]. For spiral galaxies, a single Schechter function is used with parameters including characteristic mass, normalization, and power law index specific to spiral galaxies.

For the purposes of estimating the scatter in β_E solely from the deflector dissimilarity, we neglect line-of-sight (LoS) perturbations from intervening halos, as these primarily contribute an additional stochastic scatter of $\sim 1\%$ to β_E and can be treated separately [18] while performing the cosmological forecast (see Section 5).

To ensure a realistic sample of discoverable gravitational lenses, we impose a set of detectability criteria on the simulated population following the methodology of Collett 2015 [29, Eq. 6-9]. We simulate a survey area of $20,000 \text{ deg}^2$, corresponding to the full LSST footprint. A lens system is considered detectable if it satisfies three primary conditions: multiple imaging, resolvability, and sensitivity. First, the system must produce multiple source images, requiring the unlensed source position ($r_{\text{pos}} = \sqrt{x_s^2 + y_s^2}$) to be within the Einstein radius ($\theta_E > r_{\text{pos}}$). Second, the images must be resolved from the deflector and each other. We require that the Einstein radius exceeds the effective seeing limit (FWHM), s , such that $\theta_E^2 > r_s^2 + (s/2)^2$, and that the tangential extension of the arcs is resolvable ($\mu_{\text{tot}} r_s > s$, where μ_{tot} is the total magnification). To ensure identifiable arc morphology,

²<https://github.com/LSST-strong-lensing/slsim>

we further require a total magnification of $\mu_{\text{tot}} > 3$. We adopt an optimistic seeing of $s_{\text{opt}} = 0.5''$ for LSST, assuming that strong lenses will be discovered using stacks of the best-seeing epochs (“optimal stacking”; [29]) rather than the median survey seeing of $s_{\text{med}} \approx 0.7''$ [44]; this value enters exclusively the geometric resolvability cuts described above. Finally, we impose a sensitivity cut requiring the total signal-to-noise ratio of the lensed arcs to be $\text{SNR} > 20$ in g, r, i bands following the prescription of [61] as implemented in SLSim, which uses the default `lenstronomy`³[62, 63] LSST observational configuration for per-band seeing and sky background. We further require the i -band contrast ratio > 2 (ratio of mean surface brightness of lensed source to the surface brightness of the deflector at image position) for at least 2 lensed source images. These cuts ensure that the lensed arcs are both detectable and visible against deflector light. Applying this criteria yields a parent sample (*LSST Y10*) of $\sim 116,000$ detectable galaxy-galaxy lenses across the LSST footprint, a figure consistent with the estimate of [29]. We note that utilizing the median seeing would instead yield $\sim 55,000$ lenses, which is slightly smaller than the conservative estimate of [29], attributable to our additional contrast ratio cut.

We further derive the *LSST Y1* sample from the full *LSST Y10* parent sample by modeling the accumulation of detectable lenses as a function of survey duration, specifically assuming a \sqrt{t} dependence [30]. This scaling approximates the growth in survey depth with time: as the survey accumulates exposures, the effective SNR of stacked images grows as \sqrt{t} , progressively bringing fainter arcs above the detection threshold. The Y1 sample is therefore constructed by selecting the top $\sim 37,000$ lenses ($116,000/\sqrt{10}$) with the highest SNR from the Y10 parent sample, which naturally corresponds to the brightest, most easily detectable systems that would be found first.

We define the spectroscopic follow-up sample anticipated for the 4MOST Strong Lensing Spectroscopic Legacy Survey (4SLSLS, [45]) by selecting targets from the simulated population (over $20,000 \text{ deg}^2$) that satisfy both spectroscopic feasibility and high-resolution imaging detectability. First, to ensure spectroscopic success, we impose hard selection cuts: a lensed source magnitude limit of $m_r < 24.0$ and redshift $z_S < 1.5$ to ensure that key emission lines (e.g., [OII]) from the source galaxy fall within the 4MOST wavelength coverage (370–950 nm) [45, 64]. Additionally, we require the deflector galaxy to be brighter than $m_r < 20.0$, ensuring sufficient continuum signal-to-noise for potential dynamical measurements. We then assess the detectability of these candidates assuming high-resolution imaging (effectively mimicking the joint discovery space of LSST, Euclid, and Roman) by applying the [29] detectability criteria with an optimistic seeing of $0.2''$, a signal-to-noise ratio threshold of $\text{SNR} > 20$, and no contrast ratio cut. Finally, to match the survey’s fiber allocation while maximizing scientific yield, we rank the detectable systems by their deflector r -band magnitude. We define the *4MOST* (z^{spec}) sample as the top 10,000 systems from this ranked list. For the brightest subset, the high deflector flux allows for the measurement of stellar velocity dispersions ($\sigma_{v,D}$) in addition to redshifts; thus, we define the *4MOST* ($z^{\text{spec}} + \sigma_{v,D}$) sample as the top 5,000 systems from the same ranked list.

All generated galaxy galaxy lens samples are summarized in Table 1 along with the histograms of their key properties shown in Figure 3.

4.7 Finding Self-Similar Deflector Pairs within SLSim lenses

As established in Section 4.4, photometric data constitute the most prevalent observational modality for gravitational lenses in upcoming surveys. Accordingly, our primary strategy

³<https://github.com/lenstronomy/lenstronomy>

Table 1. Description of the galaxy-galaxy lens samples generated with SLSim, drawn over an area of 20000 deg² by placing appropriate observability cuts on the lens systems. Pairing parameters for each sample are also provided below.

Sample	# Lenses	Description
LSST Y10	~116000	<p>Selection: Collett 2015 [29] cuts with $s_{\text{opt}} = 0.5''$: $\theta_E > r_{\text{pos}} = \sqrt{x_s^2 + y_s^2}$, $\theta_E > \sqrt{r_s^2 + (s_{\text{opt}}/2)^2}$, $\mu_{\text{tot}} r_s > s_{\text{opt}}$, $\mu_{\text{tot}} > 3$, $\text{SNR}_{g,r,i} > 20$, i-band contrast ratio > 2 for at least 2 images</p> <p>Pairing: $z_{\text{lens}}^{\text{photo}}$, R_e [arcsec], $f_{D,i}$, $f_{D,g}/f_{D,r}$, $f_{D,r}/f_{D,i}$</p>
LSST Y1	~37000	<p>Selection: Best SNR subset ($N_{Y1} \approx N_{Y10}/\sqrt{10}$)</p> <p>Pairing: $z_{\text{lens}}^{\text{photo}}$, R_e [arcsec], $f_{D,i}$, $f_{D,g}/f_{D,r}$, $f_{D,r}/f_{D,i}$</p>
4MOST (z^{spec})	10,000	<p>Selection: High-Res ($s = 0.2''$) detectable candi- dates (from LSST, Euclid and Roman) with: $m_{r,\text{src}} < 24.0$, $m_{r,\text{def}} < 20.0$, $z_S < 1.5$. Selected as the Top 10,000 ranked by deflector brightness ($m_{r,\text{def}}$).</p> <p>Pairing: $z_{\text{lens}}^{\text{spec}}$, R_e [arcsec], $f_{D,i}$, $f_{D,g}/f_{D,r}$, $f_{D,r}/f_{D,i}$</p>
4MOST ($z^{\text{spec}} + \sigma_{v,D}$)	5,000	<p>Selection: The Top 5,000 brightest systems from the same ranked list as the 4MOST (z^{spec}) sample (effectively the brightest 50%).</p> <p>Pairing: $z_{\text{lens}}^{\text{spec}}$, R_e [arcsec], $\sigma_{v,D}$ [km/s], $f_{D,i}$, $f_{D,g}/f_{D,r}$, $f_{D,r}/f_{D,i}$</p>

for identifying self-similar deflectors is predicated upon photometric observables and their derivative quantities. Here we evaluate the performance of three pairing strategies. The first relies exclusively on photometric parameters—redshift, size, magnitude, and colors. The second incorporates spectroscopic redshifts, where available from the 4MOST sample, alongside photometric size, magnitude, and colors. Finally, the third method combines spectroscopic redshifts and velocity dispersions with photometric size for systems in the 4MOST sample where both spectroscopic measurements are available. The list of pairing parameters used to pair deflectors for each sample is shown in Table 1. Note that we convert magnitudes/colors to fluxes or flux ratios before using them for pairing so that all pairing parameters are on a linear scale.

Prior to pairing the deflectors, it is necessary to account for uncertainties in the pairing parameters as expected from the respective surveys. According to the LSST Science Book [44], the target photometric redshift uncertainty for deflector and source galaxies is $\sigma_z/(1+z) < 0.05$, with an aspirational goal of 0.02. For simplicity, we adopt a fixed redshift uncertainty of $\sigma_z/(1+z) = 0.03$ for both deflectors and sources in all LSST Y10 lenses. For spectroscopic redshifts, we assume an uncertainty of $\sigma_z \sim 10^{-4}$, applied to both 4MOST-based samples.

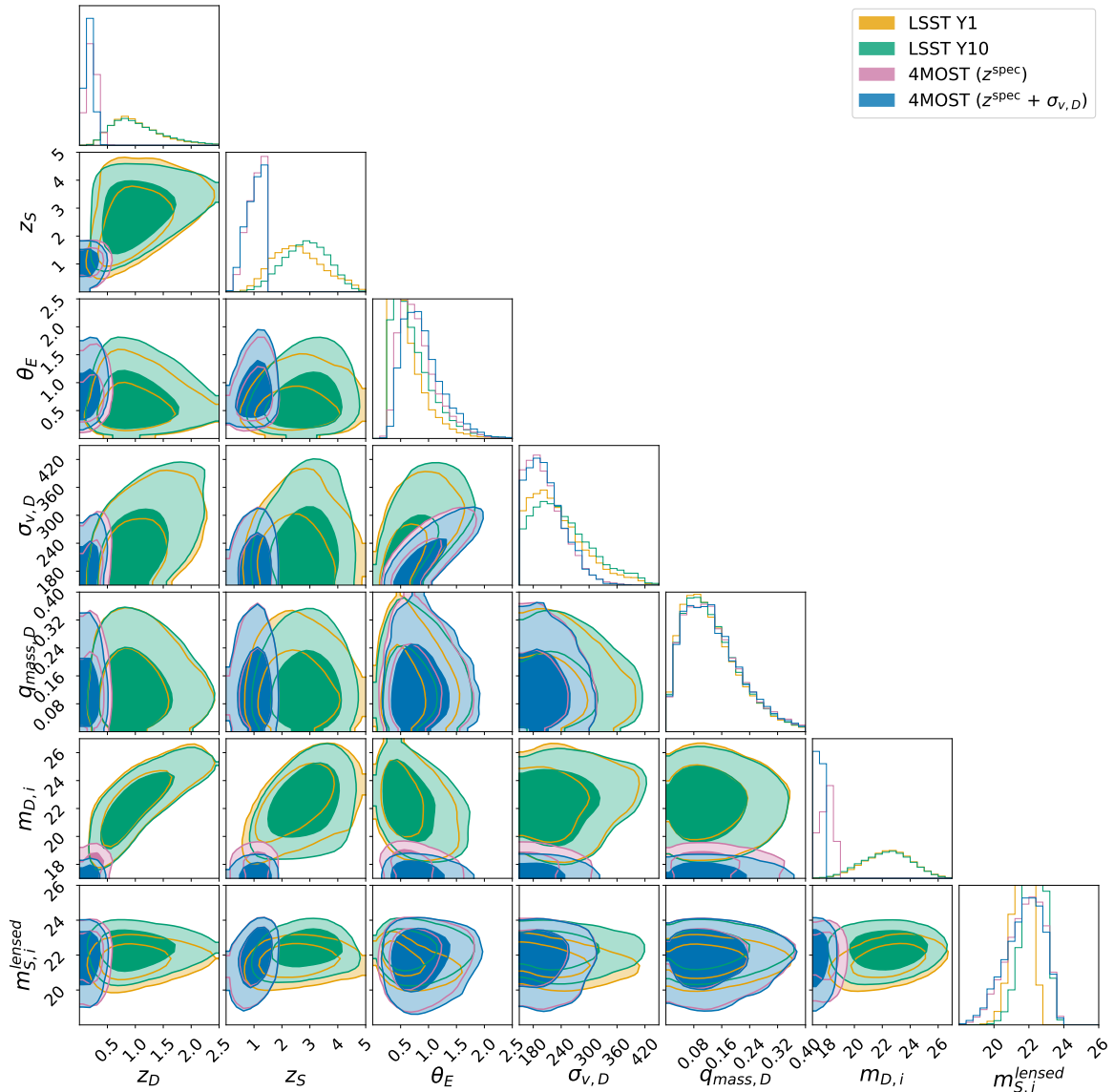


Figure 3. Population of galaxy-galaxy lenses simulated using SLSim with elliptical (red) galaxies as defectors and spiral (blue) galaxies as sources within a sky area of 20000 deg^2 . $\sigma_{v,D}$, z_D , $q_{mass,D}$, and $m_{D,i}$ represent the velocity dispersion, redshift, mass ellipticity, and i-band magnitude of the deflector galaxies, respectively, while z_S and $m_{S,i}^{lensed}$ denote the redshift and i-band magnitude of the lensed sources. θ_E represents the Einstein radius of the lens system.

Additionally, for deflector velocity dispersions, we adopt an uncertainty of 10 km s^{-1} following [64]. The size (R_e) of deflector galaxies also contains some measurement uncertainty, which we assume to be 5% here across all samples. Finally, we incorporate a photometric flux uncertainty of 1% (corresponding to ~ 10 millimags) for the deflector photometry.

The implementation of deflector pairing begins by converting photometric magnitudes into pseudo-fluxes ($f_{D,i}$) and flux ratios ($f_{D,g}/f_{D,r}$, $f_{D,r}/f_{D,i}$), defined as $f = 10^{-0.4m}$. We apply a logarithmic transformation to all strictly positive pairing features, allowing us to employ a kD-Tree data structure [65] for efficient nearest-neighbor searches in this transformed

high-dimensional space. This approach is well motivated: a Euclidean distance calculated in logarithmic space mathematically approximates the root-mean-square (RMS) fractional difference. Consequently, our **kD-Tree** algorithm directly optimizes for the dissimilarity metric ($\mathcal{D}_{\text{deflector}}$, Equation 4.8) that characterizes the scatter in our downstream cosmological likelihood. Finally, we note that as the **kD-Tree** assigns each lens its nearest neighbor independently, the resulting pairing is not a mutually exclusive 1:1 mapping, and individual lenses may appear in multiple pairs.

As previously established, identifying near-identical deflectors requires a metric based on observed properties that effectively minimizes $\Delta\beta_E/\beta_E$. While various definitions for such a metric are possible, we adopt a simplified formulation suitable for forecasting purposes. Accordingly, to quantify the degree of self-similarity between paired deflector galaxies, we employ the deflector dissimilarity parameter, defined in Equation 4.8, which takes a specific functional form depending on the sample:

$$\mathcal{D}_{\text{deflector}} \equiv \mathcal{D}_i(\text{pairing parameters}), \quad (4.9)$$

where the specific pairing parameters adopted for each sample are summarized in Table 1. As we will show, pairs with higher dissimilarity exhibit a proportionally larger scatter in their Einstein radius ratio. We parameterize this "noise floor" using a simple linear scatter model:

$$\sigma_{\beta_E, \mathcal{D}} = \sigma_{\beta_E, \mathcal{D}}^{(0)} + \sigma_{\beta_E, \mathcal{D}}^{(1)} \mathcal{D}_{\text{deflector}} \quad (4.10)$$

where $\sigma_{\beta_E, \mathcal{D}}^{(0)}$ is the baseline uncertainty for perfectly matched pairs, and $\sigma_{\beta_E, \mathcal{D}}^{(1)}$ captures the degradation as pair dissimilarity increases. While alternative functional forms could be explored for the dependence of $\sigma_{\beta_E, \mathcal{D}}$ on \mathcal{D} , the simple linear fit introduced here adequately captures these relationships across all samples tested here. This calibrated model will be directly employed when performing the cosmological forecasts in Section 5.3.

To robustly calibrate this model and quantify the overall pairing efficiency, we performed the pairing simulation 500 times for each sample. In each realization, we added random Gaussian noise to the pairing parameters consistent with the uncertainties described above and executed the **kD-Tree** matching procedure using the parameters specified in Table 1. The resulting pairing statistics—including the mean number of pairs, the mean scatter in β_E , and the best-fit coefficients for our linear scatter model—are summarized in Table 2.

To visualize these results, Figure 4 details the relative differences among key quantities for the paired deflectors. Furthermore, Figure 5 illustrates the resulting distribution of $\mathcal{D}_{\text{deflector}}$ across all samples and its correlation with the Einstein radius ratio scatter, $\sigma_{\beta_E, \mathcal{D}}$. By binning the deflector pairs at every 10th percentile in $\mathcal{D}_{\text{deflector}}$, the plot clearly demonstrates that more dissimilar pairs exhibit a proportionally higher scatter in β_E .

Comparing the survey subsets in Figure 5 reveals distinct behaviors driven by their respective observational uncertainties. The photometry-based *LSST Y10* and *LSST Y1* samples are primarily limited by photometric redshift precision. This establishes a high baseline "noise floor" ($\sigma_{\beta_E, \mathcal{D}}^{(0)} \approx 0.17\text{--}0.18$), meaning even mathematically identical pairs ($\mathcal{D}_{\text{deflector}} \rightarrow 0$) still exhibit significant scatter. Because this baseline error is dominant, the scatter exhibits a relatively shallow dependence on the dissimilarity parameter itself. Furthermore, this photo- z smearing results in a general scarcity of highly similar deflector pairs ($\mathcal{D}_{\text{deflector}} \lesssim 0.02$). However, comparing the two photometric subsets highlights the direct benefit of survey duration: the vastly larger parent sample of *LSST Y10* allows for the identification of more near-identical pairs than *LSST Y1*. This statistical advantage is evident in the marginal

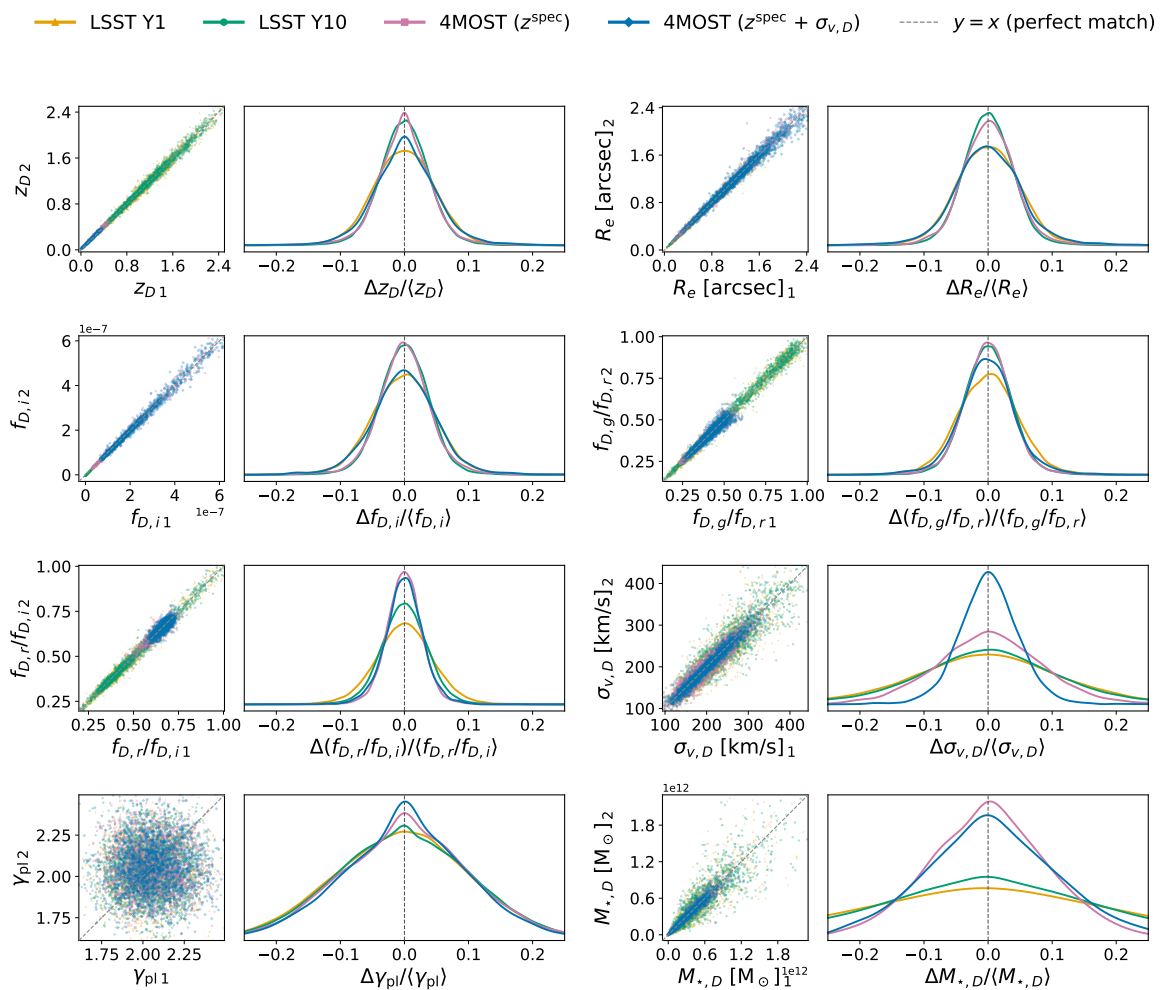


Figure 4. Pairing fidelity of deflector properties across lens samples. For each parameter/property: left panels compare values between paired deflectors (dashed gray 1:1 line); right panels show the distribution of relative fractional differences, $\Delta X/\langle X \rangle = 2(X_2 - X_1)/(X_2 + X_1)$. Rows 1–3 display pairing parameters: z_D , R_e , $f_{D,i}$, flux ratios, and $\sigma_{v,D}$. The bottom row shows residuals for γ_{pl} and stellar mass, which are not used for pairing but illustrate the matching fidelity of the physical mass models. Kinematic constraints significantly narrow the $\sigma_{v,D}$ distribution. Results represent a single representative Monte Carlo realization, similar to what’s shown in left panel of Figure 5.

distributions of Figure 5, where the $\mathcal{D}_{\text{deflector}}$ distribution for *LSST Y10* extends to notably lower values than its Y1 counterpart.

Conversely, the *4MOST* samples demonstrate a tighter average residual scatter in β_E (dropping to $\sim 8\%$). With the line-of-sight distance scatter virtually eliminated by exact spectroscopic redshifts, the remaining scatter in β_E becomes much more strongly correlated with the physical and photometric dissimilarity of the paired deflectors, resulting in a steeper linear dependence ($\sigma_{\beta_E, D}^{(1)} > 1.0$). This high-fidelity pairing is further aided by the underlying deflector population: as detailed in Section 4.6, the *4MOST* subsets select only the top 10,000 most luminous systems, which reside at the tightest end of the Lensing Mass Fundamental Plane (Section 4.5). However, this precision comes at the cost of a much smaller overall sample size.

Table 2. Summary of deflector pairing statistics for different samples. The middle three columns list the total number of lenses and resulting deflector pairs obtained over 20,000 deg², along with the corresponding fractional scatter in β_E from all the pairs. The parameters $\sigma_{\beta_E, \mathcal{D}}^{(0)}$ and $\sigma_{\beta_E, \mathcal{D}}^{(1)}$ describe a linear fit to the relation given in Equation 4.10 which quantifies how the fractional scatter in β_E varies with deflector pair dissimilarity, $\mathcal{D}_{\text{deflector}}$.

Sample	Pairing at 20K deg ²			Linear Fit	
	# Lenses	<# Pairs>	< $\Delta\beta_E/\beta_E$ >	$\sigma_{\beta_E, \mathcal{D}}^{(0)}$	$\sigma_{\beta_E, \mathcal{D}}^{(1)}$
LSST Y1	36831	27141	0.198	0.168 ± 0.002	0.63 ± 0.05
LSST Y10	116471	85819	0.193	0.180 ± 0.002	0.34 ± 0.05
4MOST (z^{spec})	10000	7324	0.078	0.029 ± 0.002	1.25 ± 0.05
4MOST ($z^{\text{spec}} + \sigma_{v,D}$)	5000	3711	0.084	0.030 ± 0.001	1.09 ± 0.02

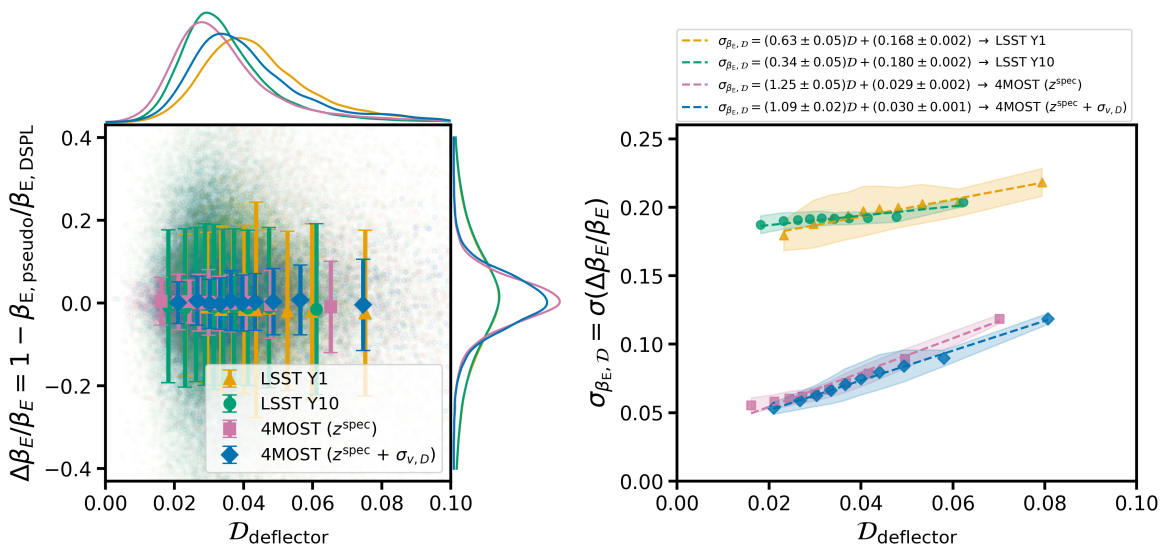


Figure 5. Simulated scatter in β_E as a function of the deflector pair dissimilarity parameter $\mathcal{D}_{\text{deflector}}$ for PDSPLs across different samples, generated with SLSim. The results summarize 500 Monte Carlo realizations accounting for measurement uncertainties on z_D , R_e , $\sigma_{v,D}$, magnitudes/fluxes, and colors/flux-ratios. *Left panel:* Individual data points and binned averages (with error bars showing the standard deviation within each bin) corresponding to a single representative realization. The marginal histograms show the distributions for this single run. *Right panel:* The mean scatter ($\sigma_{\beta_E, \mathcal{D}}$) calculated in bins corresponding to every 10th percentile, averaged over the 500 realizations. The shaded regions represent the standard deviation of the scatter across the realizations. Weighted fits to these mean scatter values are shown, with the fitted equations included in the legend. Although the definition of $\mathcal{D}_{\text{deflector}}$ (see Equation 4.8 and 4.9) varies by sample depending on the pairing parameters, it effectively represents the percentage dissimilarity between the paired deflectors.

5 Forecasts for DSPL and PDSPL with MST

5.1 Analytical error propagation

For an individual DSPL, we can do an analytical error propagation on the cosmological parameters stemming from the uncertainties in the measured Einstein radii ratio β_E , the power-law slope γ_{pl} and the MST parameter λ . In particular, a change in the inferred dark

energy equation of state parameter, δw , can be written to first order as

$$\delta w = \frac{\partial w}{\partial \beta} \left(\frac{\partial \beta}{\partial \beta_E} \delta \beta_E + \frac{\partial \beta}{\partial \lambda} \delta \lambda + \frac{\partial \beta}{\partial \gamma_{\text{pl}}} \delta \gamma_{\text{pl}} \right). \quad (5.1)$$

The partial derivatives as a function of β can be calculated from Equation 3.10. The partial derivatives around $\gamma_{\text{pl}} \approx 2$ and $\lambda \approx 1$ result in

$$\frac{\partial \beta}{\partial \beta_E} \approx 1 \quad \frac{\partial \beta}{\partial \lambda} = \frac{\partial \beta}{\partial \beta_E} \frac{\partial \beta_E}{\partial \lambda} \approx 1 - \beta_E \quad \frac{\partial \beta}{\partial \gamma_{\text{pl}}} = \frac{\partial \beta}{\partial \beta_E} \frac{\partial \beta_E}{\partial \gamma_{\text{pl}}} \approx -\beta_E \log(\beta_E). \quad (5.2)$$

The partial change in w resulting in a change from β is generally dependent on the redshift of the lens and the two sources. For typical deflector and source redshift configurations (i.e. $z_d \sim 0.5$, $z_{s1} \sim 1$, $z_{s2} \sim 2$), we get

$$\frac{\partial w}{\partial \beta} \approx -40. \quad (5.3)$$

Uncertainties in either λ or γ_{pl} directly translate to uncertainties in β and hence w . The power-law slope uncertainty is a strong function of β_E and highly suppressed for Einstein radii ratios close to one. This is expected as the change in radial density profile is a function of radial separation of the Einstein radii. The MST component λ impacts β of order unity. Constraining the MST parameter λ to one percent will enable a measurement of w to 0.4 precision.

5.2 Likelihood Function

In order to run the forecast for both the simulated DSPL and PDSPL datasets, we need to first define the Bayesian Framework. We consider a Flat $w_0 w_a$ CDM cosmology characterized by the parameters Ω_m , w_0 , and w_a , with $\Omega_\Lambda = 1 - \Omega_m$. We fix the Hubble constant to $H_0 = 70 \text{ km s}^{-1} \text{ Mpc}^{-1}$. This constraint is justified because DSPL and PDSPL observables probe ratios of angular diameter distances, rendering them independent of the absolute scale set by H_0 . We characterize this cosmology and the deflector population using the full set of model parameters Θ , and isolate the cosmological subset as Θ_c :

$$\Theta = \{H_0, \Omega_m, w_0, w_a, \bar{\lambda}_{\text{MST}}, \sigma(\lambda_{\text{MST}}), \bar{\gamma}_{\text{pl}}, \sigma(\gamma_{\text{pl}})\} \quad (5.4)$$

$$\Theta_c = \{H_0, \Omega_m, w_0, w_a\} \quad (5.5)$$

For both DSPL and PDSPL, the observable quantity is the ratio of Einstein radii, i.e., $\beta_{E, \text{meas}, i} = \theta_{E1} / \theta_{E2}$. In the case of DSPL, θ_{E1} and θ_{E2} correspond to the Einstein radii for each of the sources with the same deflector. While for the case of PDSPL, these are the Einstein radii for each of the sources with their respective deflectors. Additionally for PDSPLs, we use $z_{D,i} = \text{mean}(z_{D1,i}, z_{D2,i})$, which is a reasonable and robust approximation for self-similar deflectors.

Following the formalism introduced in Section 2, the purely geometric distance ratio $\beta_i(\Theta_c)$ depends exclusively on the cosmology and redshifts (see Equation 2.3). By modifying this geometric ratio to account for the internal mass-sheet λ_{MST} and the power-law slope γ_{pl} , the modeled Einstein radii ratio $\beta_{E, \text{pl}, i}(\Theta)$ is obtained directly from Equation 3.9.

For each DSPL or PDSPL system i , the likelihood can then be described as a Gaussian evaluated around this model prediction:

$$\mathcal{L}_i(\mathbf{D}_i | \Theta) = \frac{1}{\sqrt{2\pi\sigma_{\beta_E,i}^2(\Theta)}} \exp\left(-\frac{[\beta_{E,\text{meas},i} - \beta_{E,\text{pl},i}(\Theta)]^2}{2\sigma_{\beta_E,i}^2(\Theta)}\right) \quad (5.6)$$

where $\mathbf{D}_i = \{\beta_{E,\text{meas},i}, z_{D,i}, z_{S1,i}, z_{S2,i}\}$ represents the observed data for the i -th system, and $\sigma_{\beta_E,i}^2(\Theta)$ is the total uncertainty. To rigorously capture the error budget, we decompose this total variance into statistically independent contributions:

$$\sigma_{\beta_E,i}^2(\Theta) = \sigma_{\beta_E,\text{meas},i}^2 + \sigma_{\beta_E,\text{los},i}^2 + \sigma_{\beta_E,\mathcal{D},i}^2(\Theta) + \sigma_{\beta_E,\text{pop},i}^2(\Theta) + \sigma_{\beta_E,\text{photo-}z,i}^2(\Theta) \quad (5.7)$$

The measurement uncertainty ($\sigma_{\beta_E,\text{meas}}$) from Einstein radii measurements and the stochastic line-of-sight perturbations ($\sigma_{\beta_E,\text{los}}$) are both fixed at $\sim 1\%$ each [17, 18, 66].

For PDSPLs, the deflector self-similarity uncertainty ($\sigma_{\beta_E,\mathcal{D}}$) dominates the error budget ($\sim 8 - 20\%$). This variance, introduced by pairing two slightly dissimilar deflectors, is explicitly modeled using the dissimilarity parameter $\mathcal{D}_{\text{deflector},i}$ (see Section 4.7). Applying a linear scatter model with calibrated coefficients $\sigma_{\beta_E,\mathcal{D}}^{(0)}$ and $\sigma_{\beta_E,\mathcal{D}}^{(1)}$ (see Equation 4.10), this uncertainty scales dynamically with the model prediction:

$$\sigma_{\beta_E,\mathcal{D},i}(\Theta) = \beta_{E,\text{pl},i}(\Theta) \cdot \left(\sigma_{\beta_E,\mathcal{D}}^{(0)} + \sigma_{\beta_E,\mathcal{D}}^{(1)} \mathcal{D}_{\text{deflector},i}\right) \quad (5.8)$$

For true DSPLs, no pairing is required, thus $\sigma_{\beta_E,\mathcal{D},i} = 0$.

The population variance $\sigma_{\beta_E,\text{pop},i}^2(\Theta)$ incorporates the intrinsic scatter of the deflector mass profile parameters across the galaxy sample. It is crucial to marginalize over the structural diversity of deflectors [35] to avoid underestimating cosmological uncertainties. We parameterize this morphological variance using the intrinsic population scatters $\sigma(\lambda_{\text{MST}})$ and $\sigma(\gamma_{\text{pl}})$ (where we use $\sigma(\gamma_{\text{pl}}) \approx 0.16$ [42] and $\sigma(\lambda_{\text{MST}}) = 0.05$):

$$\sigma_{\beta_E,\text{pop},i}^2(\Theta) = \left(\frac{\partial\beta_{E,\text{pl},i}}{\partial\lambda_{\text{MST}}}\sigma(\lambda_{\text{MST}})\right)^2 + \left(\frac{\partial\beta_{E,\text{pl},i}}{\partial\gamma_{\text{pl}}}\sigma(\gamma_{\text{pl}})\right)^2 \quad (5.9)$$

Finally, the photometric redshift uncertainty term propagates the observational errors $\sigma_{x,i}$ for each redshift $x \in \{z_{D,i}, z_{S1,i}, z_{S2,i}\}$ using standard linear error propagation on the geometric ratio β_i :

$$\sigma_{\beta_E,\text{photo-}z,i}^2(\Theta) = \sum_{x \in \{z_{D,i}, z_{S1,i}, z_{S2,i}\}} \left(\frac{\partial\beta_{E,\text{pl},i}}{\partial\beta_i} \frac{\partial\beta_i}{\partial x} \sigma_{x,i}\right)^2 \quad (5.10)$$

Now using likelihoods for each system, the total likelihood for the full sample $\mathbf{D} = \{\mathbf{D}_1, \dots, \mathbf{D}_N\}$ is obtained by multiplying \mathcal{L}_i for all systems, i.e.,

$$\mathcal{L}(\mathbf{D} | \Theta) = \prod_{i=1}^N \mathcal{L}_i(\mathbf{D}_i | \Theta). \quad (5.11)$$

Finally, we implement a Bayesian hierarchical framework to constrain the model parameters at the population level. The posterior probability distribution is given by

$$p(\Theta | \mathbf{D}) \propto \mathcal{L}(\mathbf{D} | \Theta) p(\Theta) \quad (5.12)$$

where Θ denotes the set of all cosmological and deflector parameters, and \mathbf{D} represents the observational data. Wherever not specified, we choose uniform priors on the model parameters consistent with Table 3.

5.3 Simulated PDSPLs and DSPLs for forecasting

Figure 5 illustrates the scatter of $\beta_{\text{E,pseudo}}$ around $\beta_{\text{E,DSPL}}$ for **SLSim** simulated galaxy–galaxy lenses paired according to the photometric and/or spectroscopic properties of their deflectors. The observed scatter from these simulations, $\sigma_{\beta_{\text{E},\mathcal{D}}} \sim 8\text{--}20\%$, reflects intrinsic variations between the paired deflectors and the finite precision of the pairing parameters, rather than measurement uncertainties in the Einstein radii themselves, which is subdominant here. The distribution of this scatter, $\Delta\beta_{\text{E}}/\beta_{\text{E}}$, follows an approximately Gaussian form, indicating that these variations are well described by random statistical fluctuations around the true relation.

The dependence of $\sigma_{\beta_{\text{E},\mathcal{D}}}$ on the deflector dissimilarity parameter $\mathcal{D}_{\text{deflector}}$ is modeled using a linear scatter model with coefficients ($\sigma_{\beta_{\text{E},\mathcal{D}}}^{(0)}$ and $\sigma_{\beta_{\text{E},\mathcal{D}}}^{(1)}$) calibrated to the simulated sample (see Equation 4.10 and Figure 5). We use these coefficients to dynamically estimate the pairing uncertainty $\sigma_{\beta_{\text{E},\mathcal{D},i}}$ for each PDSPL system.

We forecast the constraining power of the full PDSPL population expected from LSST and 4MOST. As detailed in Table 2, the LSST Y10 sample is expected to yield tens of thousands of deflector pairs. Performing a hierarchical inference on such a massive dataset is computationally expensive. Therefore, to ensure numerical tractability while preserving the total statistical weight of the full catalog, we utilize a compressed representation of the dataset. We analyze a representative subset of systems where the log-likelihood is weighted by the sample down-sampling factor (DSF). This ensures that the width of the resulting posterior distributions accurately reflects the constraining power of the full population. We detail this numerical implementation in Appendix A.

To avoid random statistical fluctuations obscuring the true parameter constraining power, we evaluate the likelihood using Asimov datasets [67]. In an Asimov dataset, the observed mock variables ($\beta_{\text{E, meas.}}$) are set exactly to the theoretical expectation value of the true model (no stochastic Gaussian noise is added, see Appendix A), while the likelihood variance properly incorporates the full theoretical error budget. The underlying ground truth for these mocks assumes a Flat w_0w_a CDM cosmology with $\Omega_{\text{m}} = 0.3$, $w_0 = -1.0$, $w_a = 0.0$. For the mass profile population, we inject true parameters of $\bar{\gamma}_{\text{pl}} = 2.078$, $\sigma(\gamma_{\text{pl}}) = 0.16$ [42], $\bar{\lambda}_{\text{MST}} = 1.0$, and $\sigma(\lambda_{\text{MST}}) = 0.05$. The corresponding lens and source redshifts, alongside their observational uncertainties (e.g., precise spectroscopic redshifts or 3% photometric redshift errors), are adopted directly from the **SLSim** generated samples.

Finally, to directly compare the tomographic leverage of PDSPLs against DSPLs⁴, we generate an independent mock catalog of 500 genuine DSPLs—consistent with optimistic expectations for LSST Y10 [30]. Each DSPL system incorporates a joint measurement and line-of-sight precision of $\sim 1.4\%$ on the Einstein radius ratio, adopts the identical true cosmological and deflector population parameters as the PDSPLs, and utilizes exact spectroscopic redshifts.

5.4 Numerical forecast with hierarchical inference

Cosmological inference utilizing DSPL or PDSPL observables necessitates a simultaneous joint fit of the cosmological parameters alongside the population-level deflector distributions. For the PDSPL and DSPL samples outlined above, we performed a hierarchical Markov Chain Monte Carlo (MCMC) analysis. To efficiently evaluate these massive mock datasets without introducing random stochastic biases, we utilized the compressed Asimov log-likelihood

⁴We perform a simple forecast for idealized DSPLs (with no mass for the intermediate source)

framework detailed in Appendix A (which builds upon the baseline likelihood formulated in Section 5.2).

In our baseline analysis, we treat the fundamental structural diversity of the deflector population—parameterized by the intrinsic scatters $\sigma(\lambda_{\text{MST}})$ and $\sigma(\gamma_{\text{pl}})$ —as free parameters. Marginalizing over these intrinsic population scatters is essential in modern strong lensing cosmography to prevent artificially tight (and potentially biased) cosmological constraints. Conversely, for the PDSPL forecasts presented in this main text, we freeze the linear dissimilarity scatter coefficients ($\sigma_{\beta_{\text{E},\mathcal{D}}}^{(0)}$ and $\sigma_{\beta_{\text{E},\mathcal{D}}}^{(1)}$) to their pre-calibrated values. The implications of relaxing this assumption and fully self-calibrating the dissimilarity relationships directly from the data are explored extensively in Appendix C. We adopted broad uniform priors for Ω_{m} , w_0 , w_a , $\bar{\gamma}_{\text{pl}}$, $\bar{\lambda}_{\text{MST}}$, and their associated intrinsic scatters, while keeping H_0 fixed (see Table 3).

We explore the constraining power of the PDSPL samples across two main dimensions: the temporal evolution of the photometric survey (Figure 6) and the comparative advantage of spectroscopic follow-up (Figure 7) for a Flat w_0w_a CDM cosmology. As shown in Figure 6, the transition from LSST Y1 to Y10 leads to a significant contraction of the cosmological contours. Specifically, the *LSST Y10* sample yields w_0 constraints that are highly competitive and perfectly centered on the truth (as mathematically guaranteed by the Asimov formalism). This high volume photometric LSST Y10 configuration consistently outperforms the smaller spectroscopic 4MOST-based PDSPL samples, demonstrating that the sheer statistical volume of photometrically matched pairs more than compensates for the lack of spectroscopic kinematics. Conversely, the 4MOST-based samples, despite their spectroscopic precision, are fundamentally limited by sample size: the 4MOST (z^{spec}) and 4MOST ($z^{\text{spec}} + \sigma_{v,D}$) samples yield posteriors on w_0 that are broad and largely uninformative on their own ($\sigma(w_0) \gtrsim 0.7\text{--}1.0$), underscoring that 4MOST spectroscopy is most valuable as a complement to the photometric LSST Y10 sample rather than a standalone cosmological probe. The gain from progressively adding spectroscopic redshifts to the full LSST Y10 population—including a hybrid scenario where spectroscopic deflector redshifts are combined with photometric source redshifts—is explored in detail in Appendix B.

Figure 8 directly compares the PDSPL constraints from the *LSST Y10* sample against those expected from the 500 DSPL sample. We additionally overlay the constraints obtained when imposing an external Gaussian prior on the matter density, Ω_{m} of $\mathcal{N}(0.3, 0.05)$. We find that the *LSST Y10* PDSPL sample provides significantly tighter, less degenerate constraints for the dark energy equation of state compared to the 500 DSPLs. When combined with the Ω_{m} prior, the constraints on w_0 narrow considerably for the *LSST Y10* PDSPLs, effectively breaking the remaining degeneracies, whereas the standard DSPL sample remains bottlenecked by the mass-sheet degeneracy.

Beyond cosmology, our hierarchical framework successfully recovers the deflector mass profile parameters simultaneously. The inference accurately pinpoints the population mean values $\bar{\lambda}_{\text{MST}}$ and $\bar{\gamma}_{\text{pl}}$ to $\sim 2\%$ without relying on tight external priors. Additionally, we also get tight constraints on the population level intrinsic scatters $\sigma(\lambda_{\text{MST}})$ and $\sigma(\gamma_{\text{pl}})$. A comprehensive summary of the inferred posteriors—detailing the median and 1-sigma percentiles for both the cosmological and deflector parameters across all tested scenarios—is provided in Table 4.

Table 3. Parameters and their priors for the hierarchical model.

Parameters	Prior	Description
Cosmology		
H_0 [km s ⁻¹ Mpc ⁻¹]	Fixed to 70	Hubble constant
Ω_m	$\mathcal{U}(0.0, 1.0)$	Matter density
w_0	$\mathcal{U}(-3, 0)$	Dark Energy EoS
w_a	$\mathcal{U}(-5, 5)$	Dark Energy EoS
Mass profile		
$\bar{\lambda}_{\text{MST}}$	$\mathcal{U}(0.8, 1.2)$	Internal MST population mean
$\bar{\gamma}_{\text{pl}}$	$\mathcal{U}(1.0, 3.0)$	Mean power-law slope of the deflector
$\sigma(\gamma_{\text{pl}})$	$\mathcal{U}(0.0, 0.50)$	Intrinsic scatter in deflector power law slope
$\sigma(\lambda_{\text{MST}})$	$\mathcal{U}(0.0, 0.20)$	Intrinsic scatter in MST parameter

6 Discussion

The PDSPL framework proposed in this work transforms strong lensing dark energy cosmography from a regime limited by the stochastic discovery of rare alignments (DSPLs) to one driven by the statistics of wide-field surveys. By leveraging the vast population of single-source plane lenses expected from LSST, Euclid, and Roman, we trade exact geometric alignment for statistical power. In this section, we discuss the methodological advantages, strategies for refining the pair selection, the robustness of this approach against systematic uncertainties, and how this method compares against existing probes of dark energy.

First we note that our current analysis is conservative regarding the information content of the lens models. We have not accounted for the potential to break the mass-sheet degeneracy (MSD) using weak lensing constraints, as demonstrated in recent work on galaxy-scale lenses [36]. Furthermore, high-resolution imaging of lensed arcs would not only constrain the mass density slope, γ_{pl} , but also allow us to use this parameter to pair deflectors more accurately. Incorporating these priors would likely tighten the constraints on the lens population hyperparameters, further improving the cosmological precision.

6.1 Geometric Simplicity and Avoiding Intermediate Source MST

A distinct advantage of the PDSPL formalism is that it bypasses the intermediate source mass, thus avoiding the geometric and modeling complexities of true multi-source plane systems. True DSPLs suffer from “compound lensing”, where the foreground source acts as a secondary deflector for the background source, in the extreme case creating complex “Einstein zig-zag” geometries [24, 68]. Modeling these systems requires computationally expensive multi-plane ray tracing and introduces additional free parameters. More critically, this intermediate source introduces its own independent, unmeasurable mass-sheet degeneracy. Breaking this secondary degeneracy requires virtually impossible spatially resolved kinematics, severely limiting the robustness of derived cosmological constraints. To put the magnitude of this systematic into perspective, literature explicitly modelling genuine DSPLs (such as SDSSJ0946+1006) demonstrates that the intermediate source is not a passive tracer, but a secondary deflector with a non-negligible Einstein radius (e.g., $\theta_E \approx 0.15''$; [17, 68]). As

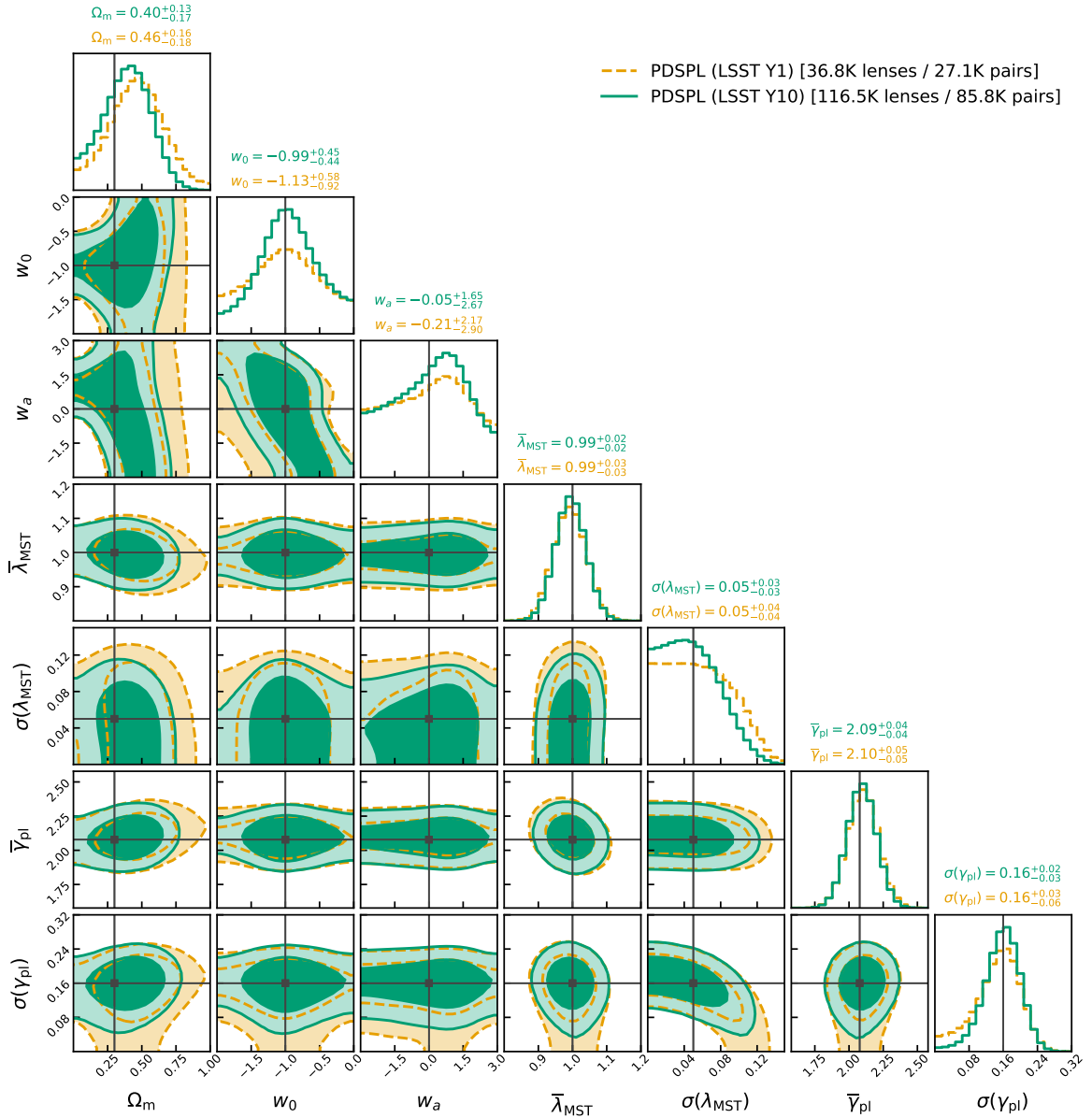


Figure 6. Comparison of posterior distributions for the LSST Y1 (orange) and LSST Y10 (green) PDSPL samples, illustrating the impact of survey duration on cosmological constraints in a Flat $w_0 w_a$ CDM cosmology. The transition to the full Y10 sample size ($\sim 86,000$ pairs) significantly reduces parameter degeneracies. Contours represent 68% and 95% confidence levels, with the ground truth indicated by black lines.

shown by these studies, failing to account for this compound lensing effect biases the inferred deflector mass profile and geometric distance ratios by several percent. Given the sensitivity of the dark energy equation of state to these ratios, such an unmodeled systematic bias would severely degrade the cosmological constraining power of any standard DSPL sample. PDSPLs circumvent this bottleneck by design. By pairing two *independent* single-source plane lenses, there is no intermediate mass to model and no secondary mass-sheet degeneracy to break. This cleanly isolates the cosmological signal in the angular diameter distance ratios, free from

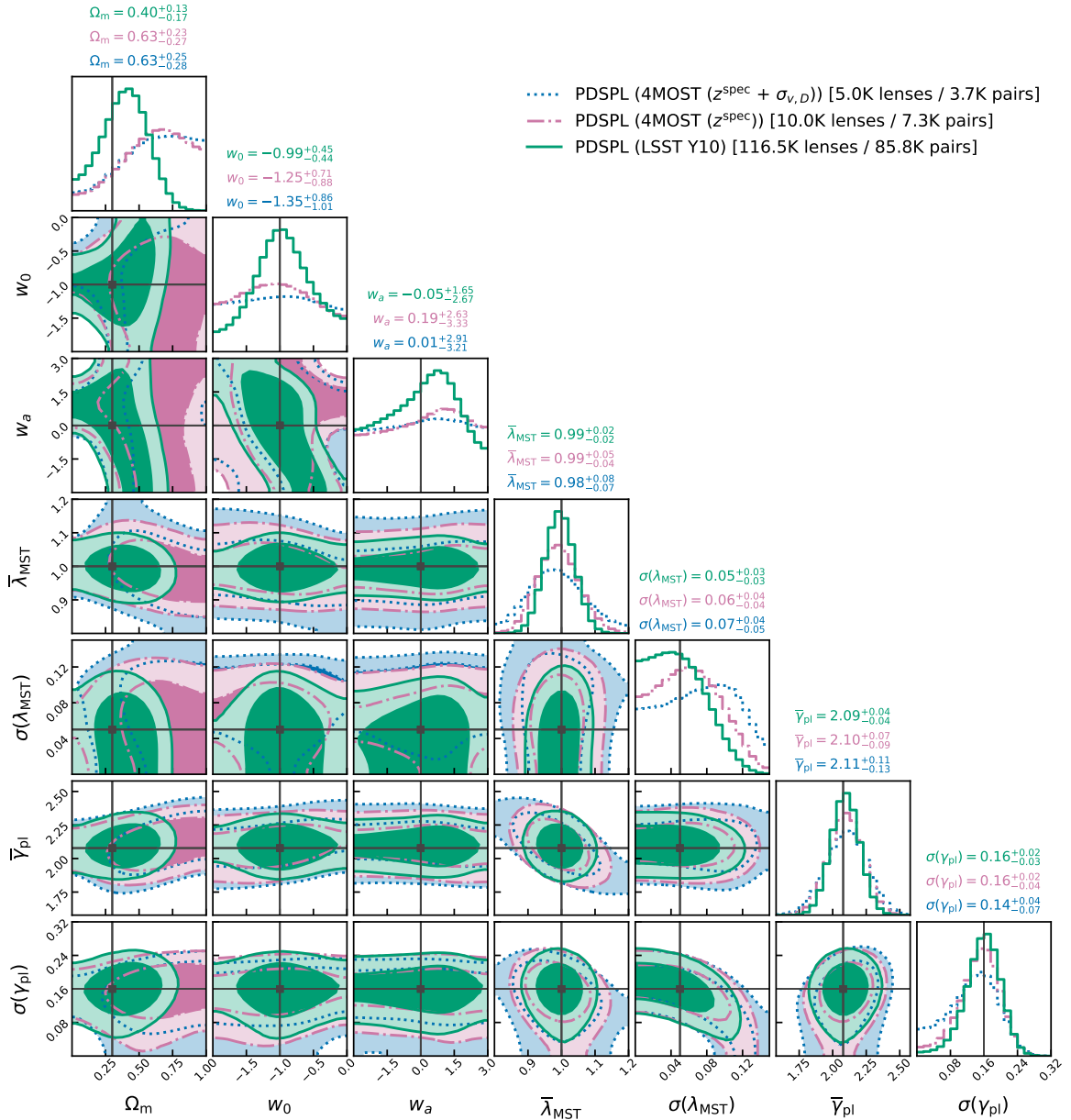


Figure 7. Comparison of LSST Y10 photometric samples against spectroscopic 4MOST-based PDSPL subsets. Despite the high fidelity pairing with the 4MOST measurements (z^{spec} and $\sigma_{v,D}$), the significantly larger statistical volume of the LSST Y10 photometric sample provides tighter overall constraints on w_0 and w_a in a Flat $w_0 w_a$ CDM cosmology. Contours represent 68% and 95% confidence levels, with the ground truth indicated by black lines.

the confounding effects of lens-lens coupling. Ultimately, avoiding the intermediate source MST ensures more robust constraints and drastically simplifies likelihood evaluation—a crucial optimization for processing the $\mathcal{O}(10^5)$ systems expected from next-generation surveys.

6.2 Observational Yield and Survey Constraints

The statistical power of the PDSPL methodology is fundamentally tied to the number of detectable lens systems. Consequently, the constraints forecasted in this work are sensitive

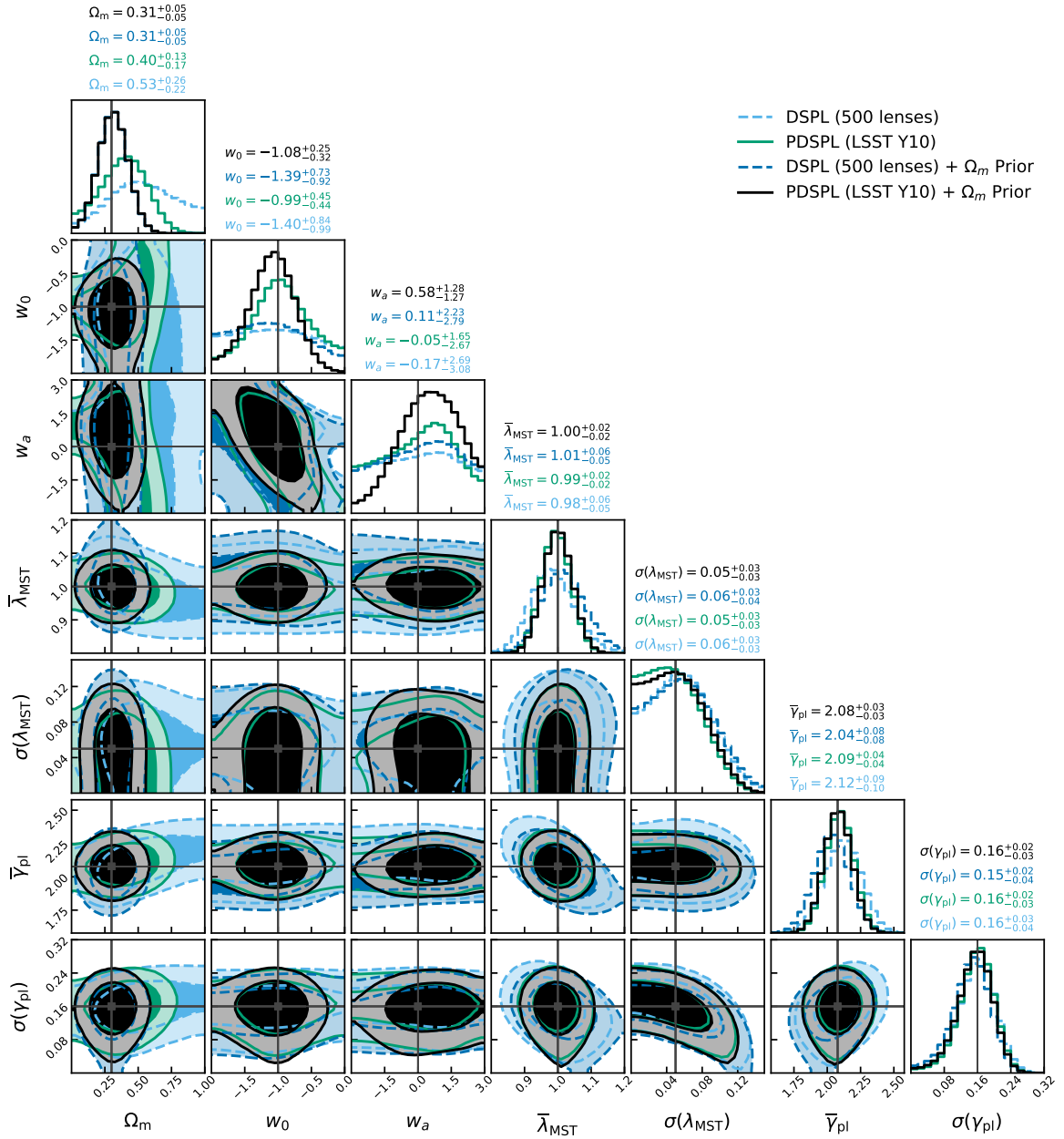


Figure 8. Comparison of posterior distributions for the DSPL (500 lenses) and LSST Y10 PDSPL samples while inferring Flat w_0w_a CDM cosmology. Results are shown both with and without an external prior on Ω_m of $\mathcal{N}(0.3, 0.05)$. The PDSPL sample (solid green/black contours) demonstrates significantly tighter constraints on the dark energy equation of state parameters (w_0, w_a) compared to the standard DSPL sample (dashed blue contours). Ground truth is also shown with black horizontal/vertical lines. Note that the DSPL (500 lenses) shows an idealized case where the forecast assumes no mass of the intermediate source.

to the practical observational realities of upcoming wide-field surveys.

Sensitivity to Survey Seeing Conditions: The baseline forecast assumes optimal stacking with $s_{\text{opt}} = 0.5''$, representing an optimistic but physically motivated scenario where strong lenses are discovered from stacks of the best-seeing epochs [29]. Under median survey seeing ($s_{\text{med}} \approx$

0.7"), the detectable lens sample reduces to $\sim 55,000$ systems (Section 4.6), and the number of deflector pairs scales accordingly. Assuming the constraining power scales as $\sigma(w_0) \propto N_{\text{pairs}}^{-1/2}$, this corresponds to a degradation of $\sim 1.4\times$, yielding $\sigma(w_0) \sim 0.62$ without an Ω_m prior. The baseline $s_{\text{opt}} = 0.5''$ result should therefore be understood as an upper bound on the statistical performance, with the median-seeing case representing a plausible conservative scenario.

Detectability of Compact Lenses and Space-Based Synergy: While our theoretical detectability criteria in Section 4.6 allows for inclusion of lenses down to $\theta_E \sim 0.25''$ (Figure 3), identifying such compact systems solely from ground-based imaging is highly ambitious. Automated search algorithms typically degrade near the seeing limit, making $\theta_E \lesssim 0.5''$ lenses exceptionally challenging to confidently identify [69, 70]. However, morphological verification of these smaller systems will become feasible using optimally drizzled data and, crucially, high-resolution space-based imaging [71]. Since the Roman High Latitude Wide Area Survey (HLWAS) and Euclid Wide Survey heavily overlap with the LSST footprint [72, 73], leveraging these space-based observations will be essential to confirm compact lens candidates and preserve the large statistical volume required for the PDSPL methodology. Moreover these space based observatories may provide more precise measurements of the Einstein Radii, thus helping with the cosmology.

6.3 Optimizing Deflector Pairing

The constraining power of the PDSPL method is defined by the "noise floor" introduced by deflector dissimilarity. Our analysis highlights three avenues to suppress this noise and improve the fidelity of the observable β_E .

The Conservative Nature of the Noise Floor: It is important to emphasize that the constraints presented in this work are likely conservative. Our forecast relies on the pairing scatter $\sigma_{\beta_E, \mathcal{D}}$ derived from simulations, which may not fully capture the tightness of the scaling relations governing real galaxy populations. For instance, the existence of a Mass Fundamental Plane (MFP, [43]) implies that galaxies are tightly correlated in the multidimensional space of lensing mass density, size, and velocity dispersion. Furthermore, established empirical correlations demonstrate that the mass density power-law slope γ_{pl} is physically linked to the macroscopic structure of galaxies, specifically their size (effective radius) and central mass density (e.g., as shown in the SLACS X analysis by [42]; see their Figure 5). Because central mass density and size are directly derived from photometric imaging, purely photometric matching implicitly selects for similar underlying mass profiles. If real galaxy populations adhere to these tighter scaling relations, the intrinsic scatter between photometrically matched pairs will naturally be lower than our simulated "noise floor", $\sigma_{\beta_E, \mathcal{D}}$. This would allow the PDSPL method to achieve even higher precision relying solely on imaging statistics, a prospect that upcoming wide-field surveys will be perfectly positioned to empirically validate. Furthermore, as evidenced by our *4MOST* mock samples (Figure 5), this noise floor can be actively suppressed by strategically restricting PDSPL pairings to the brightest, most massive deflector candidates where these scaling relations are tightest, trading raw sample volume for higher-fidelity individual pairs.

Refining Matches with Spectroscopy: While the PDSPL method does not fundamentally rely on spectroscopic data, incorporating precise spectroscopic redshifts (z_D^{spec}) serves as a powerful tool to further suppress the intrinsic pairing scatter. As demonstrated in our analysis (see Figure 5), replacing photometric redshifts with spectroscopic ones significantly improves the matching fidelity. This improvement arises because the Einstein radius ratio (β_E) is highly sensitive to the angular diameter distances of the lenses; eliminating photo- z uncertainties removes a major source of line-of-sight distance scatter. Consequently, obtaining z_D^{spec} mea-

measurements for the full LSST Y10 deflector population would be highly beneficial—it would simultaneously lower the systematic pairing noise floor and remove the photometric error budget from the likelihood evaluation, yielding sharper constraints on the dark energy equation of state (as detailed in Appendix B). Interestingly, we find that incorporating central velocity dispersion ($\sigma_{v,D}$) constraints alongside z_D^{spec} yields no further significant reduction in the scatter. This indicates that precise redshift matching, when combined with high-quality photometric structural parameters, is largely sufficient to pair self-similar mass profiles. Furthermore, it highlights a distinct advantage of the PDSPL framework: unlike traditional methods that depend heavily on kinematics for absolute mass calibration, any available kinematic data here serves strictly to refine the deflector pairing process. Achieving this for the full LSST Y10 population will require dedicated wide-field spectroscopic campaigns. Imminent surveys such as WAVES@4MOST [74] and, on a 10–15 year timescale, proposed facilities like the 12 metre Wide-field Spectroscopic Telescope [WST; 75] with $\sim 30,000$ fibres represent realistic pathways to delivering spectroscopic redshifts for the full LSST strong lens population within the survey lifetime.

Anisotropic Dissimilarity Weighting: In our current formulation (Equation 4.8), the dissimilarity parameter $\mathcal{D}_{\text{deflector}}$ is calculated as an unweighted Euclidean distance in normalized parameter space. This implicitly treats a 1σ deviation in redshift as equivalent to a 1σ deviation in magnitude. However, the sensitivity of β_E to these parameters is physically anisotropic; variations in deflector redshift directly alter the angular diameter distance ratios, impacting β_E more severely than photometric fluctuations. While a simple weighted distance metric ($\mathcal{D}^2 = \sum w_k (\Delta P_k)^2$) could account for these differential sensitivities, it ignores the fact that key photometric/spectroscopic observables may possess significant intrinsic covariances [76]. Consequently, future iterations of this methodology should employ a fully generalized Mahalanobis-like distance metric [77]. This approach would incorporate both the Fisher information content of each parameter relative to β_E and the physical correlations between the observables themselves, yielding a statistically optimal pairing strategy.

Morphological Matching via Deep Learning: Finally, our current kD-Tree matching relies on scalar catalog observables (redshift, magnitude, radius, colors or velocity dispersion), discarding the rich morphological information contained in pixel-level data. With the advent of high-resolution imaging from space based surveys like Euclid and Roman, future implementations could employ deep learning techniques, such as contrastive learning, to perform "image-level" matching. These methods can identify morphological analogs by capturing higher-order structural features that escape parametric fits, increasing the effective sample size of high-fidelity pairs.

6.4 Self-Calibration of $\sigma_{\beta_E, \mathcal{D}}$

In this forecasting analysis, we characterized the expected scatter $\sigma_{\beta_E, \mathcal{D}}$ using the SLSim pipeline. However, the application of PDSPLs to observational data need not rely rigidly on simulation-derived noise models. Given the large sample sizes expected from LSST, the PDSPL framework supports a hierarchical Bayesian analysis where the intrinsic scatter arising from deflector dissimilarity is treated as a free hyperparameter. Rather than fixing $\sigma_{\beta_E, \mathcal{D}}$ to a theoretical model/value, it can be inferred simultaneously with the cosmological and deflector parameters. This “self-calibration” approach ensures that constraints remain robust even if the true covariance of the galaxy population differs from simulated predictions. See Appendix C where we simultaneously infer the dissimilarity scatter on β_E for LSST Y10 PDSPL sample.

6.5 Synergy with External Datasets

As shown in Figure 8, the PDSPL method is most powerful when combined with external probes that constrain the matter density Ω_m , such as the Cosmic Microwave Background (e.g., Planck [78]), Baryon Acoustic Oscillations (e.g., DESI [1]), or Type Ia Supernovae (e.g., Pantheon+ [79]). The synergy between the geometric probe of PDSPLs (sensitive to expansion history) and the growth-of-structure probes (sensitive to Ω_m) highlights the role of strong lensing tomography as a complementary pillar of precision cosmology.

6.6 Systematic Uncertainties

While the PDSPL framework bypasses the modeling complexities of true multi-source plane systems, it is susceptible to unique systematic uncertainties that collectively dictate its irreducible “noise floor”, $\sigma_{\beta_E, \mathcal{D}}$:

Photometric-to-Mass Mapping: The assumption that similar photometry implies identical mass profiles carries intrinsic, irreducible scatter (e.g., varying dark matter fractions) that translates directly into uncertainty on β_E .

Environmental Variations: Pairing structurally identical galaxies that reside in different local environments (e.g., field vs. cluster) introduces unmodeled differences in external convergence (κ_{ext}) and shear, elevating the baseline 1% line-of-sight scatter [18].

Photo- z Errors and Galaxy Evolution: Large photometric redshift uncertainties risk pairing deflector galaxies across different cosmic epochs, potentially introducing biases from the structural evolution of elliptical galaxies over time.

Selection Bias: Survey detectability criteria (e.g., minimum θ_E , SNR limits, etc.) [29] preferentially select lenses that scatter upward in deflection angle. Crucially for PDSPLs, this effect is redshift-dependent: an identical deflector requires a more extreme upward mass scatter to clear the detectability threshold if its source is at a lower redshift due to lower geometric lensing efficiency. This Malmquist-like bias systematically skews the inferred population mass parameters ($\bar{\gamma}_{\text{pl}}$, $\bar{\lambda}_{\text{MST}}$), directly propagating errors into the cosmological constraints unless rigorously corrected via forward-modeling.

Astrophysical Contaminants and Profile Assumptions: The PDSPL framework relies on the stability of deflector mass profiles and clean photometry. Photometric contamination from luminous Active Galactic Nuclei (AGN) is expected to be minimal in massive early-type galaxies [80], and any such anomalous systems would naturally be rejected during color-based pairing. Structurally, while massive ellipticals may possess flattened inner stellar cores, the *total* enclosed mass at the typical Einstein radius remains robustly well-described by a near-isothermal power law [81]. Finally, for spectroscopic pairing, typical fiber apertures (e.g., 1.5'' for 4MOST [82]) subtend kiloparsec scales at typical deflector redshifts. This far exceeds the supermassive black hole (SMBH) sphere of influence, ensuring that measured velocity dispersions trace the global stellar halo and remain unaffected by the intrinsic scatter in SMBH scaling relations.

6.7 Comparison with Literature and the Impact of Degeneracies

It is instructive to place the PDSPL methodology in the context of other strong lensing probes of dark energy, particularly those leveraging the statistical power of upcoming surveys like LSST and Euclid. Recent forecasts for “Lensing + Kinematics” demonstrate the potential of combining Einstein radius measurements with stellar kinematics for large populations. [64] show that a sample of 10,000 lenses from Euclid/4MOST can constrain the equation of

state to $\sigma(w) \approx 0.11$ in Flat w CDM. However, this method relies heavily on the absolute calibration of the kinematic measurements; constraints degrade significantly if the velocity dispersion precision worsens (e.g., from 10 km/s) or if there are systematic uncertainties in the stellar anisotropy models. Similarly, Time Delay Cosmography (TDC) offers robust constraints; [83] forecast that a sample of ~ 800 lensed AGN from LSST can yield a dark energy Figure of Merit (FoM) of 6.7. While powerful, TDC requires resource-intensive long-term monitoring campaigns to achieve high-precision time delays and is sensitive to the "mass-sheet transformation" degeneracy.

In contrast, the PDSPL framework leverages relative measurements between pairs of deflector galaxies. By comparing two deflectors, we aim to cancel out systematic uncertainties associated with the absolute mass calibration that limit single-lens methods. While PDSPLs provide looser constraints per system than TDC or Lensing+Dynamics, the sheer volume of available pairs allows for a self-calibration of the lens population hyperparameters (such as λ_{MST} and γ_{pl}) that is difficult to achieve with smaller samples.

Previous analyses of Double Source Plane Lenses (DSPLs), such as [84], have demonstrated that a sample of 87 DSPLs can constrain the dark energy equation of state to $w_0 = -1.09_{-0.32}^{+0.31}$ within a Flat $w_0 w_a$ CDM framework, provided that the mass-sheet parameter λ_{MST} and density slope γ_{pl} are fixed or tight priors are assumed. However, we demonstrate that when these parameters are treated as free variables in a full hierarchical inference, the constraining power of the limited DSPL sample is substantially degraded due to the mass-sheet degeneracy. We find that the PDSPL methodology—applied to the photometrically selected LSST Y10 sample—recovers constraints of $w_0 = -0.99_{-0.44}^{+0.45}$ with uniform priors. Crucially, this precision is achieved while simultaneously constraining the population hyperparameters.

Finally, compared to weak lensing tomography, our constraints on w_0 for the LSST 10-year PDSPL sample with Ω_m prior ($w_0 = -1.08_{-0.32}^{+0.25} \rightarrow \sigma(w_0) \sim 0.29$) are comparable to current Stage III cosmic shear surveys, such as the Dark Energy Survey (DES) Y3 3×2 pt analysis which yields $w_0 = -0.98_{-0.20}^{+0.32}$ [85]. This demonstrates that the PDSPL technique can extract a cosmological signal from strong lensing that is competitive with established large-scale structure probes.

7 Conclusion

In this work, we have introduced and characterized the framework of Pseudo Double Source Plane Lenses (PDSPLs) as a novel probe for dark energy. By relaxing the requirement for rare, multi-source plane alignments and instead pairing independent single-source plane lenses with self-similar deflectors, we unlock the statistical potential of the $\sim 10^5$ strong lenses expected from upcoming wide-field surveys.

We derived the transformation of the double-source plane observable (the Einstein radius ratio, β_E) under the Mass-Sheet Degeneracy (MSD). We explicitly showed that β_E is degenerate with the internal mass sheet parameter λ_{MST} and the power-law slope γ_{pl} . This highlights that precise cosmological inference requires either breaking the MSD or marginalizing over it within a hierarchical framework.

Using simulations from the SLSim pipeline, we quantified the "noise floor" introduced by pairing distinct deflectors. We note that these estimates may be conservative if the real galaxy population adheres to a tighter Mass Fundamental Plane than assumed in our simulations. We found that while the inclusion of spectroscopic information for finding near-identical

deflector significantly reduces the intrinsic scatter in β_E (from $\sim 19\%$ to $\sim 8\%$), the cosmological constraining power is ultimately driven by sample size. Consequently, the massive photometric sample expected from LSST yields tighter constraints than the smaller, high-fidelity spectroscopic subset achievable with campaigns like 4MOST. This confirms that the PDSPL method is robustly viable using imaging survey statistics alone, without relying on spectroscopic follow-up efforts (which could certainly help).

The cosmological forecasts presented here demonstrate that PDSPLs can yield constraints on the dark energy equation of state parameters that surpass those from current samples of genuine DSPLs. Specifically, we found that:

- A limited sample of 500 genuine DSPLs is severely limited by the mass-sheet degeneracy, yielding loose constraints of $w_0 = -1.39^{+0.73}_{-0.92}$ even with an Ω_m prior, when marginalizing over mass profile parameters.
- In contrast, the photometrically selected PDSPL sample from LSST Y10 ($\sim 10^5$ pairs) provides sufficient statistical leverage to self-calibrate the population, achieving a precision of $\sigma(w_0) \sim 0.45$ in a Flat $w_0 w_a$ CDM cosmology. This constraint further tightens to $\sigma(w_0) \sim 0.29$ when combined with a Gaussian prior of $\mathcal{N}(0.3, 0.05)$ on the matter density (Ω_m), demonstrating the strong synergy between PDSPLs and external growth-of-structure probes.
- The large sample size of PDSPLs allows for the simultaneous constraint of the population-level mass profile parameters including their intrinsic population scatters, determining the mean internal mass sheet λ_{MST} and power-law slope γ_{pl} to a precision of $\sim 2\%$ compared to a precision of $\sim 5\%$ from 500 DSPLs.

To contextualise these results, our best constraint of $\sigma(w_0) \sim 0.29$ (with an Ω_m prior) is comparable to current Stage III cosmic shear surveys such as DES Y3 [85]. Together with other strong lensing probes of dark energy—such as lensing+kinematics [64] and time-delay cosmography with lensed quasars [83]—PDSPLs provide a complementary and statistically powerful avenue that exploits the galaxy-galaxy lens catalogs that LSST, Euclid, and Roman will naturally produce. We note that the systematic effects discussed in Section 6 are not yet incorporated into these forecasts and will need to be addressed in future work. Ultimately, by converting the abundant population of standard galaxy-galaxy lenses into a tomographic dataset, the PDSPL formalism positions strong lensing tomography as a statistics-driven, self-calibrating probe of cosmic expansion in the era of next-generation surveys.

Acknowledgments

This paper has undergone a joint internal review in the LSST Dark Energy Science Collaboration (DESC) and the Strong Lensing Science Collaboration (SLSC). The internal reviewers were Tian Li and Adam Bolton, and they provided extremely valuable feedback that helped improve the robustness of the analysis and the draft.

Contribution Statement: SB proposed the pseudo-DSPL concept, developed the initial formalism, and outlined the manuscript. PS generated the simulated lens populations, devised pairing technique, performed the cosmological forecasting and analysis, and wrote the final manuscript. NK contributed to the configuration and implementation of the `SLSim` pipeline for sample generation. SE, PH, PM, DDN, CT, and BW provided extensive feedback on the initial analysis and the manuscript.

Software: The source code for this work is publicly available at the github repository [pdspl-analysis](#). This work makes use of the publicly available softwares: [SLSim](#) [57], [hierarc](#) [35], and [emcee](#) [86].

Funding: PS and SB are supported by DoE Grant DE-SC0026113. SB acknowledges support by Schmidt Futures. SE acknowledges funding from NSF GRFP 2021313357. SE and PM performed work under DOE Contract DE-AC02-76SF00515. TL is funded by the European Research Council (ERC) under the European Union’s Horizon 2020 research and innovation program (LensEra: grant agreement No 945536). TA acknowledges support from ANID-FONDECYT Regular Project 1240105 and the ANID BASAL project FB210003. GPS acknowledges support from The Royal Society, the Leverhulme Trust and the Science and Technology Facilities Council (grant number ST/X001296/1).

The DESC acknowledges ongoing support from the Institut National de Physique Nucléaire et de Physique des Particules in France; the Science & Technology Facilities Council in the United Kingdom; and the Department of Energy and the LSST Discovery Alliance in the United States. DESC uses resources of the IN2P3 Computing Center (CC-IN2P3–Lyon/Villeurbanne - France) funded by the Centre National de la Recherche Scientifique; the National Energy Research Scientific Computing Center, a DOE Office of Science User Facility supported by the Office of Science of the U.S. Department of Energy under Contract No. DE-AC02-05CH11231; STFC DiRAC HPC Facilities, funded by UK BEIS National E-infrastructure capital grants; and the UK particle physics grid, supported by the GridPP Collaboration. This work was performed in part under DOE Contract DE-AC02-76SF00515.

References

- [1] A.G. Adame, J. Aguilar, S. Ahlen, S. Alam, D.M. Alexander, M. Alvarez et al., *DESI 2024 VI: cosmological constraints from the measurements of baryon acoustic oscillations*, *JCAP* **2025** (2025) 021 [[2404.03002](#)].
- [2] Z. Zhang, T. Xu and Y. Chen, *Dynamical Dark Energy and the Unresolved Hubble Tension: Multi-model Constraints from DESI 2025 and Other Probes*, *ApJ* **999** (2026) 248 [[2512.07281](#)].
- [3] J. de Cruz Pérez, A. Gómez-Valent and J. Solà Peracaula, *Dynamical dark energy models in light of the latest observations*, *Phys. Rev. D* **113** (2026) 083521 [[2512.20616](#)].
- [4] E. Di Valentino, O. Mena, S. Pan, L. Visinelli, W. Yang, A. Melchiorri et al., *In the realm of the Hubble tension—a review of solutions*, *Classical and Quantum Gravity* **38** (2021) 153001 [[2103.01183](#)].
- [5] E. Abdalla, G.F. Abellán, A. Aboubrahim, A. Agnello, Ö. Akarsu, Y. Akrami et al., *Cosmology intertwined: A review of the particle physics, astrophysics, and cosmology associated with the cosmological tensions and anomalies*, *Journal of High Energy Astrophysics* **34** (2022) 49 [[2203.06142](#)].
- [6] M. Chevallier and D. Polarski, *Accelerating Universes with Scaling Dark Matter*, *International Journal of Modern Physics D* **10** (2001) 213 [[gr-qc/0009008](#)].
- [7] E.V. Linder and A. Jenkins, *Cosmic structure growth and dark energy*, *MNRAS* **346** (2003) 573 [[astro-ph/0305286](#)].
- [8] R.R. Caldwell and E.V. Linder, *Limits of Quintessence*, *Phys. Rev. Lett.* **95** (2005) 141301 [[astro-ph/0505494](#)].
- [9] S. Singh and P. Singh, *It’s a dark, dark world: background evolution of interacting ϕ CDM models beyond simple exponential potentials*, *JCAP* **2016** (2016) 017 [[1507.01535](#)].

- [10] G.-B. Zhao, M. Raveri, L. Pogosian, Y. Wang, R.G. Crittenden, W.J. Handley et al., *Dynamical dark energy in light of the latest observations*, *Nature Astronomy* **1** (2017) 627 [[1701.08165](#)].
- [11] B. Jain and A. Taylor, *Cross-Correlation Tomography: Measuring Dark Energy Evolution with Weak Lensing*, *PRL* **91** (2003) 141302 [[astro-ph/0306046](#)].
- [12] W. Hu, *Dark energy and matter evolution from lensing tomography*, *Phys. Rev. D* **66** (2002) 083515 [[astro-ph/0208093](#)].
- [13] Dark Energy Survey and Kilo-Degree Survey Collaboration, T.M.C. Abbott, M. Agüena, A. Alarcon, O. Alves, A. Amon et al., *DES Y3 + KiDS-1000: Consistent cosmology combining cosmic shear surveys*, *The Open Journal of Astrophysics* **6** (2023) 36 [[2305.17173](#)].
- [14] E. Jullo, P. Natarajan, J.-P. Kneib, A. D’Aloisio, M. Limousin, J. Richard et al., *Cosmological constraints from strong gravitational lensing in clusters of galaxies.*, *Science* **329** (2010) 924 [[1008.4802](#)].
- [15] G.B. Caminha, S.H. Suyu, C. Grillo and P. Rosati, *Galaxy cluster strong lensing cosmography. Cosmological constraints from a sample of regular galaxy clusters*, *A&A* **657** (2022) A83 [[2110.06232](#)].
- [16] R. Gavazzi, T. Treu, L.V.E. Koopmans, A.S. Bolton, L.A. Moustakas, S. Burles et al., *The Sloan Lens ACS Survey. VI. Discovery and Analysis of a Double Einstein Ring*, *ApJ* **677** (2008) 1046 [[0801.1555](#)].
- [17] T.E. Collett and M.W. Auger, *Cosmological constraints from the double source plane lens SDSSJ0946+1006*, *MNRAS* **443** (2014) 969 [[1403.5278](#)].
- [18] D. Johnson, T. Collett, T. Li and P. Fleury, *Line-of-sight effects on double source plane lenses*, *arXiv e-prints* (2025) arXiv:2501.17153 [[2501.17153](#)].
- [19] N. Sahu, A.J. Shajib, K.-V. Tran, H. Skobe, S. Rhoades, T. Jones et al., *Cosmography with the Double-source-plane Strong Gravitational Lens AGEL150745+052256*, *ApJ* **991** (2025) 72 [[2504.00656](#)].
- [20] D.J. Bowden, N. Sahu, A.J. Shajib, K.-V. Tran, T.M. Barone, K.V. G. C. et al., *Constraining Cosmology with Double-source-plane Strong Gravitational Lenses from the AGEL Survey*, *ApJ* **993** (2025) 124 [[2509.15012](#)].
- [21] M. Tanaka, K.C. Wong, A. More, A. Dezuka, E. Egami, M. Oguri et al., *A Spectroscopically Confirmed Double Source Plane Lens System in the Hyper Suprime-Cam Subaru Strategic Program*, *ApJL* **826** (2016) L19 [[1606.09363](#)].
- [22] K. Wong, “HST Imaging of the Eye of Horus, a Double Source Plane Gravitational Lens.” HST Proposal id.15325. Cycle 25, Aug., 2017.
- [23] K. Tanaka, A. Tsuji, H. Akamatsu, J.H.H. Chan, J. Coupon, E. Egami et al., *X-ray study of the double source plane gravitational lens system Eye of Horus observed with XMM-Newton*, *MNRAS* **491** (2020) 3411 [[1911.04805](#)].
- [24] F. Dux, M. Millon, C. Lemon, T. Schmidt, F. Courbin, A.J. Shajib et al., *J1721+8842: The first Einstein zigzag lens*, *A&A* **694** (2025) A300 [[2411.04177](#)].
- [25] E. Collaboration, T. Li, T.E. Collett, M. Walmsley, N.E.P. Lines, K. Rojas et al., *Euclid quick data release (q1). the strong lensing discovery engine d – double-source-plane lens candidates*, 2025.
- [26] Ž. Ivezić, S.M. Kahn, J.A. Tyson, B. Abel, E. Acosta, R. Allsman et al., *LSST: From Science Drivers to Reference Design and Anticipated Data Products*, *ApJ* **873** (2019) 111 [[0805.2366](#)].
- [27] R. Laureijs, J. Amiaux, S. Arduini, J.L. Auguères, J. Brinchmann, R. Cole et al., *Euclid Definition Study Report*, *arXiv e-prints* (2011) arXiv:1110.3193 [[1110.3193](#)].

- [28] D. Spergel, N. Gehrels, C. Baltay, D. Bennett, J. Breckinridge, M. Donahue et al., *Wide-Field Infrared Survey Telescope-Astrophysics Focused Telescope Assets WFIRST-AFTA 2015 Report*, *arXiv e-prints* (2015) arXiv:1503.03757 [1503.03757].
- [29] T.E. Collett, *The Population of Galaxy-Galaxy Strong Lenses in Forthcoming Optical Imaging Surveys*, *ApJ* **811** (2015) 20 [1507.02657].
- [30] A.J. Shajib, G.P. Smith, S. Birrer, A. Verma, N. Arendse, T. Collett et al., *Strong gravitational lenses from the Vera C. Rubin Observatory*, *Philosophical Transactions of the Royal Society of London Series A* **383** (2025) 20240117 [2406.08919].
- [31] G. Ferrami and J.S.B. Wyithe, *A model for galaxy-galaxy strong lensing statistics in surveys*, *MNRAS* **532** (2024) 1832 [2404.03143].
- [32] B. Wedig, T. Daylan, S. Birrer, F.-Y. Cyr-Racine, C. Dvorkin, D.P. Finkbeiner et al., *The Roman View of Strong Gravitational Lenses*, *ApJ* **986** (2025) 42 [2506.03390].
- [33] E.E. Falco, M.V. Gorenstein and I.I. Shapiro, *On model-dependent bounds on H_0 from gravitational images : application to Q 0957+561 A, B.*, *ApJL* **289** (1985) L1.
- [34] P. Schneider, *Can one determine cosmological parameters from multi-plane strong lens systems?*, *A&A* **568** (2014) L2 [1406.6152].
- [35] S. Birrer, A.J. Shajib, A. Galan, M. Millon, T. Treu, A. Agnello et al., *TDCOSMO. IV. Hierarchical time-delay cosmography - joint inference of the Hubble constant and galaxy density profiles*, *A&A* **643** (2020) A165 [2007.02941].
- [36] N. Khadka, S. Birrer, A. Leauthaud and H. Nix, *Breaking the mass-sheet degeneracy in strong lensing mass modelling with weak lensing observations*, *MNRAS* **533** (2024) 795 [2404.01513].
- [37] M.V. Gorenstein, E.E. Falco and I.I. Shapiro, *Degeneracies in Parameter Estimates for Models of Gravitational Lens Systems*, *ApJ* **327** (1988) 693.
- [38] P. Schneider and D. Sluse, *Mass-sheet degeneracy, power-law models and external convergence: Impact on the determination of the Hubble constant from gravitational lensing*, *A&A* **559** (2013) A37 [1306.0901].
- [39] S. Birrer, A. Amara and A. Refregier, *The mass-sheet degeneracy and time-delay cosmography: analysis of the strong lens RXJ1131-1231*, *JCAP* **2016** (2016) 020 [1511.03662].
- [40] A. Sonnenfeld, *On the choice of lens density profile in time delay cosmography*, *MNRAS* **474** (2018) 4648 [1710.05925].
- [41] C.S. Kochanek, *Overconstrained gravitational lens models and the Hubble constant*, *MNRAS* **493** (2020) 1725 [1911.05083].
- [42] M.W. Auger, T. Treu, A.S. Bolton, R. Gavazzi, L.V.E. Koopmans, P.J. Marshall et al., *The Sloan Lens ACS Survey. X. Stellar, Dynamical, and Total Mass Correlations of Massive Early-type Galaxies*, *ApJ* **724** (2010) 511 [1007.2880].
- [43] P. Mozumdar, S. Knabel, T. Treu, A. Sonnenfeld, A.J. Shajib, M. Cappellari et al., *XXII. Accurate stellar velocity dispersions of the SL2S lens sample and the lensing mass fundamental plane*, *arXiv e-prints* (2025) arXiv:2505.13962 [2505.13962].
- [44] LSST Science Collaboration, P.A. Abell, J. Allison, S.F. Anderson, J.R. Andrew, J.R.P. Angel et al., *LSST Science Book, Version 2.0*, *arXiv e-prints* (2009) arXiv:0912.0201 [0912.0201].
- [45] T.E. Collett, A. Sonnenfeld, C. Frohmaier, K. Glazebrook, D. Sluse, V. Motta et al., *The 4MOST Strong Lensing Spectroscopic Legacy Survey (4SLSLS)*, *The Messenger* **190** (2023) 49.
- [46] S. Djorgovski and M. Davis, *Fundamental Properties of Elliptical Galaxies*, *ApJ* **313** (1987) 59.
- [47] A. Dressler, D. Lynden-Bell, D. Burstein, R.L. Davies, S.M. Faber, R. Terlevich et al., *Spectroscopy and Photometry of Elliptical Galaxies. I. New Distance Estimator*, *ApJ* **313** (1987) 42.

- [48] S.M. Faber and R.E. Jackson, *Velocity dispersions and mass-to-light ratios for elliptical galaxies.*, *ApJ* **204** (1976) 668.
- [49] J. Kormendy, *Brightness distributions in compact and normal galaxies. II. Structure parameters of the spheroidal component.*, *ApJ* **218** (1977) 333.
- [50] R.G. Bower, J.R. Lucey and R.S. Ellis, *Precision photometry of early-type galaxies in the Coma and Virgo clusters : a test of the universality of the colour-magnitude relation - I. The data.*, *MNRAS* **254** (1992) 589.
- [51] A. Gallazzi, S. Charlot, J. Brinchmann, S.D.M. White and C.A. Tremonti, *The ages and metallicities of galaxies in the local universe*, *MNRAS* **362** (2005) 41 [[astro-ph/0506539](#)].
- [52] L. Ferrarese and D. Merritt, *A Fundamental Relation between Supermassive Black Holes and Their Host Galaxies*, *ApJL* **539** (2000) L9 [[astro-ph/0006053](#)].
- [53] K. Gebhardt, R. Bender, G. Bower, A. Dressler, S.M. Faber, A.V. Filippenko et al., *A Relationship between Nuclear Black Hole Mass and Galaxy Velocity Dispersion*, *ApJL* **539** (2000) L13 [[astro-ph/0006289](#)].
- [54] A.S. Bolton, S. Burles, T. Treu, L.V.E. Koopmans and L.A. Moustakas, *A More Fundamental Plane*, *ApJL* **665** (2007) L105 [[astro-ph/0701706](#)].
- [55] A. Gargiulo, C.P. Haines, P. Merluzzi, R.J. Smith, F. La Barbera, G. Busarello et al., *On the origin of the scatter around the Fundamental Plane: correlations with stellar population parameters*, *MNRAS* **397** (2009) 75 [[0902.4383](#)].
- [56] L.-B. Desroches, E. Quataert, C.-P. Ma and A.A. West, *Luminosity dependence in the Fundamental Plane projections of elliptical galaxies*, *MNRAS* **377** (2007) 402 [[astro-ph/0608474](#)].
- [57] N. Khadka, S. Birrer, H. Best, P. Sharma, K.T. Abe, X. Tang et al., *SLSim: a strong lensing population simulation package*, *arXiv e-prints* (2026) [arXiv:2603.17138](#) [[2603.17138](#)].
- [58] P. Schechter, *An analytic expression for the luminosity function for galaxies.*, *ApJ* **203** (1976) 297.
- [59] A. Amara, L. de la Bella, S. Birrer, S. Bridle, J. Cordero, G. Favole et al., *SkyPy: A package for modelling the Universe*, *The Journal of Open Source Software* **6** (2021) 3056 [[2109.06172](#)].
- [60] M. Bernardi, F. Shankar, J.B. Hyde, S. Mei, F. Marulli and R.K. Sheth, *Galaxy luminosities, stellar masses, sizes, velocity dispersions as a function of morphological type*, *MNRAS* **404** (2010) 2087 [[0910.1093](#)].
- [61] P. Holloway, A. Verma, P.J. Marshall, A. More and M. Tecza, *On the detectability of strong lensing in near-infrared surveys*, *MNRAS* **525** (2023) 2341 [[2308.00851](#)].
- [62] S. Birrer and A. Amara, *lenstronomy: Multi-purpose gravitational lens modelling software package*, *Physics of the Dark Universe* **22** (2018) 189 [[1803.09746](#)].
- [63] S. Birrer, A. Shajib, D. Gilman, A. Galan, J. Aalbers, M. Millon et al., *lenstronomy II: A gravitational lensing software ecosystem*, *The Journal of Open Source Software* **6** (2021) 3283 [[2106.05976](#)].
- [64] T. Li, T.E. Collett, C.M. Krawczyk and W. Enzi, *Cosmology from large populations of galaxy-galaxy strong gravitational lenses*, *MNRAS* **527** (2024) 5311 [[2307.09271](#)].
- [65] P. Virtanen, R. Gommers, T.E. Oliphant, M. Haberland, T. Reddy, D. Cournapeau et al., *SciPy 1.0: Fundamental Algorithms for Scientific Computing in Python*, *Nature Methods* **17** (2020) 261.
- [66] R.J. Smith and T.E. Collett, *A fully-spectroscopic triple-source-plane lens: the Jackpot completed*, *MNRAS* **505** (2021) 2136 [[2104.12790](#)].

- [67] G. Cowan, K. Cranmer, E. Gross and O. Vitells, *Asymptotic formulae for likelihood-based tests of new physics*, *European Physical Journal C* **71** (2011) 1554 [[1007.1727](#)].
- [68] T.E. Collett and D.J. Bacon, *Compound lensing: Einstein zig-zags and high-multiplicity lensed images*, *MNRAS* **456** (2016) 2210 [[1510.00242](#)].
- [69] A. Herle, C.M. O’Riordan and S. Vegetti, *Selection functions of strong lens finding neural networks*, *MNRAS* **534** (2024) 1093 [[2307.10355](#)].
- [70] R. Cañameras, S. Schuldt, Y. Shu, S.H. Suyu, S. Taubenberger, I.T. Andika et al., *HOLISMOKES: XI. Evaluation of supervised neural networks for strong-lens searches in ground-based imaging surveys*, *A&A* **692** (2024) A72 [[2306.03136](#)].
- [71] E. Silver, R. Wang, X. Huang, A.S. Bolton, C.J. Storfer and S. Banka, *ML-driven Strong Lens Discoveries: Down to $\theta_E \sim 0.''03$ and $M_{\text{halo}} < 10^{11} M_{\odot}$* , *ApJ* **994** (2025) 117 [[2507.01943](#)].
- [72] P. Capak, J.-C. Cuillandre, F. Bernardeau, F. Castander, R. Bowler, C. Chang et al., *Enhancing LSST Science with Euclid Synergy*, *arXiv e-prints* (2019) [arXiv:1904.10439](#) [[1904.10439](#)].
- [73] R. Observations Time Allocation Committee and C. Community Survey Definition Committees, *Roman Observations Time Allocation Committee: Final Report and Recommendations*, *arXiv e-prints* (2025) [arXiv:2505.10574](#) [[2505.10574](#)].
- [74] G. Kaur, M. Bilicki, S. Bellstedt, E. Tempel, W.A. Hellwing, I. Baldry et al., *Wide Area VISTA Extragalactic Survey (WAVES): Selection of targets for the Wide survey using decision-tree classification*, *arXiv e-prints* (2025) [arXiv:2510.11132](#) [[2510.11132](#)].
- [75] V. Mainieri, R.I. Anderson, J. Brinchmann, A. Cimatti, R.S. Ellis, V. Hill et al., *The Wide-field Spectroscopic Telescope (WST) Science White Paper*, *arXiv e-prints* (2024) [arXiv:2403.05398](#) [[2403.05398](#)].
- [76] M. Bernardi, R.K. Sheth, J. Annis, S. Burles, D.J. Eisenstein, D.P. Finkbeiner et al., *Early-type Galaxies in the Sloan Digital Sky Survey. II. Correlations between Observables*, *AJ* **125** (2003) 1849 [[astro-ph/0301624](#)].
- [77] P. Mahalanobis, *On the Generalised Distance in Statistics.*, *Sankhya A* **80** (2018) 1–7.
- [78] Planck Collaboration, N. Aghanim, Y. Akrami, M. Ashdown, J. Aumont, C. Baccigalupi et al., *Planck 2018 results. VI. Cosmological parameters*, *A&A* **641** (2020) A6 [[1807.06209](#)].
- [79] D. Brout, D. Scolnic, B. Popovic, A.G. Riess, A. Carr, J. Zuntz et al., *The Pantheon+ Analysis: Cosmological Constraints*, *ApJ* **938** (2022) 110 [[2202.04077](#)].
- [80] G. Kauffmann, T.M. Heckman, C. Tremonti, J. Brinchmann, S. Charlot, S.D.M. White et al., *The host galaxies of active galactic nuclei*, *MNRAS* **346** (2003) 1055 [[astro-ph/0304239](#)].
- [81] L.V.E. Koopmans, A. Bolton, T. Treu, O. Czoske, M.W. Auger, M. Barnabè et al., *The Structure and Dynamics of Massive Early-Type Galaxies: On Homology, Isothermality, and Isotropy Inside One Effective Radius*, *ApJL* **703** (2009) L51 [[0906.1349](#)].
- [82] R.S. de Jong, O. Bellido-Tirado, C. Chiappini, É. Depagne, R. Haynes, D. Johl et al., *4MOST: 4-metre multi-object spectroscopic telescope*, in *Ground-based and Airborne Instrumentation for Astronomy IV*, I.S. McLean, S.K. Ramsay and H. Takami, eds., vol. 8446 of *Society of Photo-Optical Instrumentation Engineers (SPIE) Conference Series*, p. 84460T, Sept., 2012, DOI [[1206.6885](#)].
- [83] S. Erickson, M. Millon, P. Venkatraman, T. Li, P. Holloway, P. Marshall et al., *Investigating the Dark Energy Constraint from Strongly Lensed AGN at LSST-Scale*, *arXiv e-prints* (2025) [arXiv:2511.13669](#) [[2511.13669](#)].
- [84] D. Sharma, T.E. Collett and E.V. Linder, *Testing cosmology with double source lensing*, *JCAP* **2023** (2023) 001 [[2212.00055](#)].

- [85] T.M.C. Abbott, M. Aguena, A. Alarcon, S. Allam, O. Alves, A. Amon et al., *Dark Energy Survey Year 3 results: Cosmological constraints from galaxy clustering and weak lensing*, *Phys. Rev. D* **105** (2022) 023520 [[2105.13549](#)].
- [86] D. Foreman-Mackey, D.W. Hogg, D. Lang and J. Goodman, *emcee: The mcmc hammer*, *PASP* **125** (2013) 306 [[1202.3665](#)].

Table 4. Cosmological forecast constraints for the PDSPL samples and 500 DSPLs.

Sample	Ω_m	w_0	w_a	$\bar{\lambda}_{\text{MST}}$	$\sigma(\lambda_{\text{MST}})$	$\bar{\gamma}_{\text{pl}}$	$\sigma(\gamma_{\text{pl}})$
TRUTH	0.30	-1.00	0.00	1.000	0.050	2.078	0.160
Flat w_0w_aCDM							
DSPL (500 lenses)	$0.53^{+0.26}_{-0.22}$	$-1.40^{+0.84}_{-0.99}$	$-0.17^{+2.69}_{-3.08}$	$0.981^{+0.056}_{-0.046}$	$0.056^{+0.033}_{-0.033}$	$2.123^{+0.088}_{-0.104}$	$0.163^{+0.025}_{-0.036}$
PDSPL (LSST Y1)	$0.46^{+0.16}_{-0.18}$	$-1.13^{+0.58}_{-0.92}$	$-0.21^{+2.17}_{-2.90}$	$0.992^{+0.028}_{-0.026}$	$0.054^{+0.040}_{-0.037}$	$2.104^{+0.049}_{-0.051}$	$0.157^{+0.026}_{-0.058}$
PDSPL (LSST Y10)	$0.40^{+0.13}_{-0.17}$	$-0.99^{+0.45}_{-0.44}$	$-0.05^{+1.65}_{-2.67}$	$0.994^{+0.019}_{-0.019}$	$0.045^{+0.031}_{-0.030}$	$2.094^{+0.035}_{-0.032}$	$0.164^{+0.017}_{-0.032}$
PDSPL (4MOST z^{spec})	$0.63^{+0.23}_{-0.27}$	$-1.25^{+0.71}_{-0.88}$	$0.19^{+2.63}_{-3.33}$	$0.988^{+0.051}_{-0.044}$	$0.059^{+0.035}_{-0.036}$	$2.103^{+0.073}_{-0.085}$	$0.156^{+0.025}_{-0.043}$
PDSPL (4MOST $z^{\text{spec}} + \sigma_v$)	$0.63^{+0.25}_{-0.28}$	$-1.35^{+0.86}_{-1.01}$	$0.01^{+2.91}_{-3.21}$	$0.983^{+0.082}_{-0.070}$	$0.074^{+0.040}_{-0.048}$	$2.108^{+0.110}_{-0.127}$	$0.142^{+0.040}_{-0.070}$
Flat w_0w_aCDM + Ω_m prior[†]							
DSPL (500 lenses)	$0.31^{+0.05}_{-0.05}$	$-1.39^{+0.73}_{-0.92}$	$0.11^{+2.23}_{-2.79}$	$1.013^{+0.056}_{-0.048}$	$0.056^{+0.035}_{-0.035}$	$2.036^{+0.083}_{-0.084}$	$0.150^{+0.024}_{-0.036}$
PDSPL (LSST Y1)	$0.31^{+0.05}_{-0.05}$	$-1.13^{+0.39}_{-0.61}$	$0.67^{+1.55}_{-1.72}$	$1.001^{+0.028}_{-0.027}$	$0.061^{+0.037}_{-0.040}$	$2.076^{+0.044}_{-0.045}$	$0.148^{+0.028}_{-0.061}$
PDSPL (LSST Y10)	$0.31^{+0.05}_{-0.05}$	$-1.08^{+0.25}_{-0.32}$	$0.58^{+1.28}_{-1.27}$	$0.999^{+0.018}_{-0.018}$	$0.048^{+0.032}_{-0.032}$	$2.081^{+0.030}_{-0.030}$	$0.160^{+0.017}_{-0.034}$
PDSPL (4MOST z^{spec})	$0.31^{+0.05}_{-0.05}$	$-1.05^{+0.57}_{-0.65}$	$0.76^{+1.58}_{-2.15}$	$1.016^{+0.056}_{-0.050}$	$0.059^{+0.037}_{-0.037}$	$2.043^{+0.090}_{-0.089}$	$0.147^{+0.025}_{-0.044}$
PDSPL (4MOST $z^{\text{spec}} + \sigma_v$)	$0.31^{+0.05}_{-0.05}$	$-1.17^{+0.74}_{-0.91}$	$0.45^{+2.24}_{-2.80}$	$1.026^{+0.087}_{-0.084}$	$0.075^{+0.038}_{-0.049}$	$2.020^{+0.145}_{-0.131}$	$0.129^{+0.040}_{-0.068}$

[†] The prior on Ω_m is $\mathcal{N}(0.3, 0.05)$.

A Numerical compression and Asimov forecasting

To efficiently forecast constraints for populations exceeding 10^5 systems, we emulate the statistical power of the large PDSPL samples using smaller, computationally tractable representative subsets. For a full sample of size N_{total} represented by a subset of size N_{subset} , we define a Down-Sampling Factor (DSF) as $\text{DSF} = N_{\text{total}}/N_{\text{subset}}$.

To prevent random stochastic fluctuations from shifting or biasing the inferred parameter posteriors, we evaluate the likelihood using Asimov datasets [67]. An Asimov dataset replaces the randomized observational data with the exact theoretical expectation of the true underlying model.

For a Gaussian likelihood where the variance itself is a function of the proposed model parameters Θ , the expected value of the log-likelihood must account for the true underlying variance of the data. Let $\beta_{\text{E, true},i}$ and $\sigma_{\text{true},i}^2$ represent the true Einstein radius ratio and the true total variance injected into the i -th mock system, respectively. The expectation value of the squared residuals evaluated at a proposed model $\beta_{\text{E, pl},i}(\Theta)$ is analytically given by:

$$\mathbb{E} \left[(\beta_{\text{E, meas},i} - \beta_{\text{E, pl},i}(\Theta))^2 \right] = \sigma_{\text{true},i}^2 + (\beta_{\text{E, true},i} - \beta_{\text{E, pl},i}(\Theta))^2 \quad (\text{A.1})$$

Substituting this expectation into the standard Gaussian log-likelihood yields the exact Asimov log-likelihood for a single system:

$$\ln \mathcal{L}_i^{\text{Asimov}}(\Theta) = -\frac{1}{2} \left[\frac{\sigma_{\text{true},i}^2 + (\beta_{\text{E, true},i} - \beta_{\text{E, pl},i}(\Theta))^2}{\sigma_{\beta_{\text{E},i}}^2(\Theta)} + \ln(2\pi\sigma_{\beta_{\text{E},i}}^2(\Theta)) \right] \quad (\text{A.2})$$

where $\sigma_{\beta_{\text{E},i}}^2(\Theta)$ is the parameter-dependent variance defined in Section 5.2. Note that when the proposed model parameters perfectly match the truth ($\Theta = \Theta_{\text{true}}$), the residual term vanishes and $\sigma_{\beta_{\text{E},i}}^2(\Theta) = \sigma_{\text{true},i}^2$, thereby maximizing the likelihood exactly at the injected truth.

To rigorously preserve the total information and statistical weight of the full catalog while evaluating only a subset, we uniformly scale the log-likelihood of each system in the representative subset by the DSF. The total compressed Asimov log-likelihood becomes:

$$\ln \mathcal{L}_{\text{tot}}^{\text{Asimov}}(\Theta) = \sum_{i=1}^{N_{\text{subset}}} \text{DSF} \times \ln \mathcal{L}_i^{\text{Asimov}}(\Theta) \quad (\text{A.3})$$

This scaling ensures that the likelihood—and thus the width of the resulting marginal posterior distributions—scales identically to that of the full population, which narrows proportionally to $1/\sqrt{N_{\text{total}}}$. This approach allows for highly accurate, unbiased parameter constraint estimations while significantly reducing the computational overhead of the Markov Chain Monte Carlo (MCMC) sampling.

B The Impact of Spectroscopic Redshifts on PDSPL Cosmology

While our baseline forecasts demonstrate the viability of PDSPLs using purely photometric data, widespread spectroscopic follow-up represents the theoretical ideal. Incorporating precise spectroscopic redshifts enhances the PDSPL framework through two distinct pathways: First, at the pairing stage, exact deflector redshifts (z_D^{spec}) drastically improve the fidelity of the kD-Tree algorithm. Removing photo- z errors reduces the intrinsic mismatch between

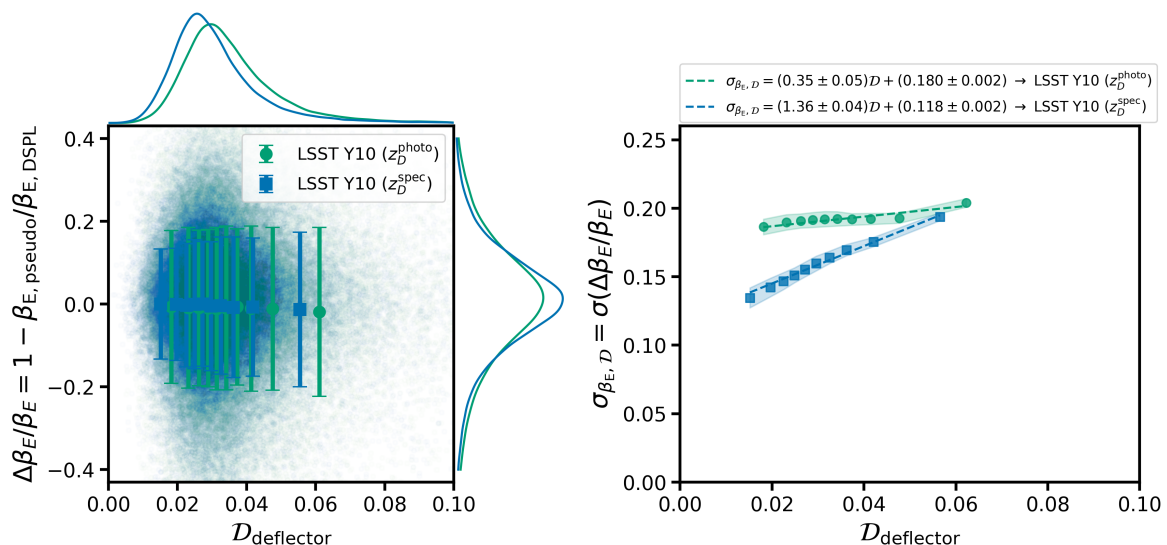


Figure 9. Simulated scatter in β_E as a function of deflector pair dissimilarity ($\mathcal{D}_{\text{deflector}}$) for the LSST Y10 sample (formatting is same as in Figure 5). Replacing photometric deflector redshifts (green) with exact spectroscopic redshifts (blue) significantly improves pairing fidelity, lowering the baseline noise floor ($\sigma_{\beta_E, \mathcal{D}}$). Because the pairing procedure incorporates random observational errors, the linear fit coefficients for the LSST Y10 (z_D^{photo}) sample exhibit slight numerical variations across the 500 Monte Carlo realizations compared to the values reported in the main text.

paired lenses, suppressing the average dissimilarity noise floor ($\sigma_{\beta_E, \mathcal{D}}$) from $\sim 19\%$ to $\sim 15\%$, as shown in Figure 9. Notably, even with perfect redshift knowledge, this LSST Y10 noise floor remains higher than that of the 4MOST (z^{spec}) sample’s average noise ($\sim 8\%$, see Figure 5). This discrepancy stems entirely from the underlying deflector populations: whereas the 4MOST subset is strictly limited to massive, highly luminous ellipticals that tightly adhere to the Mass Fundamental Plane (Section 6.3), the full LSST Y10 catalog includes a long tail of fainter, lower-mass galaxies with greater intrinsic structural diversity. Second, at the cosmological inference stage, exact redshifts eliminate the photometric error budget ($\sigma_{\text{photo}-z}$, Equation 5.10) propagated into the geometric distance ratio (β) during likelihood evaluation. Figure 10 demonstrates this dual impact on our full LSST Y10 forecast ($\sim 86,000$ pairs). Progressing sequentially from a purely photometric baseline ($z_D^{\text{phot}}, z_S^{\text{phot}}$) to a hybrid sample ($z_D^{\text{spec}}, z_S^{\text{phot}}$) and finally to an idealized fully spectroscopic sample ($z_D^{\text{spec}}, z_S^{\text{spec}}$) systematically tightens the dark energy equation of state constraints.

C Inferring Dissimilarity Scatter $\sigma_{\beta_E, \mathcal{D}}$

In our baseline analysis presented in the main text, the parameters governing the linear dissimilarity scatter model ($\sigma_{\beta_E, \mathcal{D}}^{(0)}$ and $\sigma_{\beta_E, \mathcal{D}}^{(1)}$) were fixed to the values calibrated from our **SLSim** simulations (Table 2). We refer to this baseline configuration as the **“Fixed Scatter”** model. However, given the vast statistical volume of the LSST Y10 PDSPL sample, it is possible to treat these systematic noise parameters as free variables and infer them simultaneously with the cosmology and deflector population properties. We refer to this fully self-calibrating configuration as the **“Free Scatter”** model.

This “self-calibration” approach ensures that the cosmological constraints remain robust even if the true variance of the observational sample differs from our simulated assumptions. To

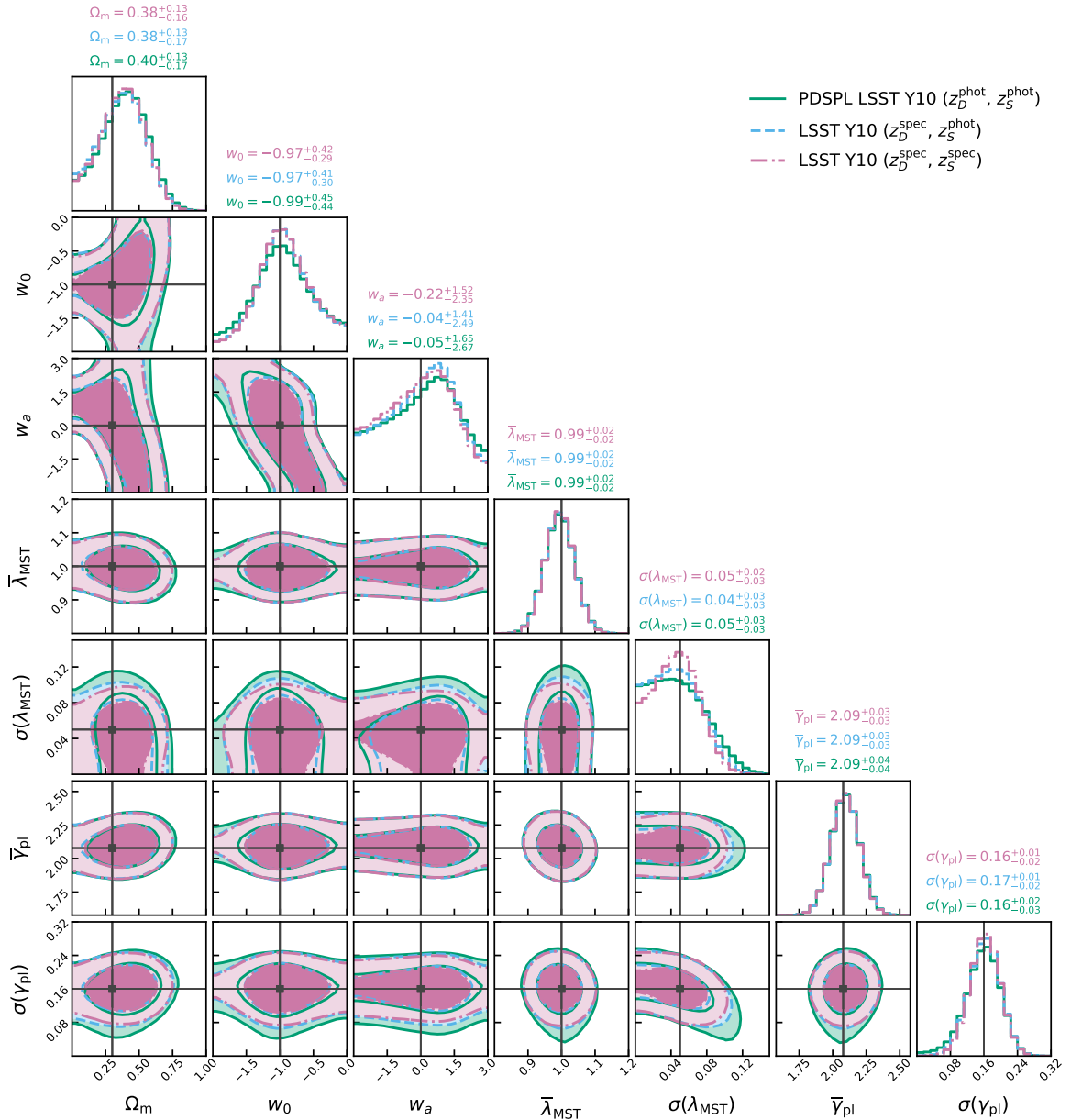


Figure 10. Forecasted posterior distributions for the LSST Y10 PDSPL sample illustrating the impact of spectroscopic redshifts on cosmological constraints. The contours show the 68% and 95% confidence levels for a Flat $w_0 w_a$ CDM cosmology. The baseline photometric configuration (green) is compared against scenarios where exact spectroscopic redshifts are available for the deflectors only (dashed blue) and for both the deflectors and sources (dash dotted pink). The progressive inclusion of spectroscopic data tightens the constraints on w_0 and w_a by simultaneously lowering the pairing noise floor and eliminating line-of-sight distance uncertainties.

test this, we performed a hierarchical inference on the LSST Y10 mock catalog adopting broad uniform priors for the scatter coefficients. Figure 11 displays the resulting posteriors, demonstrating that the massive sample size successfully constrains the systematic noise floor without external calibration. Figure 12 provides a direct comparison between the fixed-scatter and free-scatter inferences. We find that when freeing the scatter parameters, the

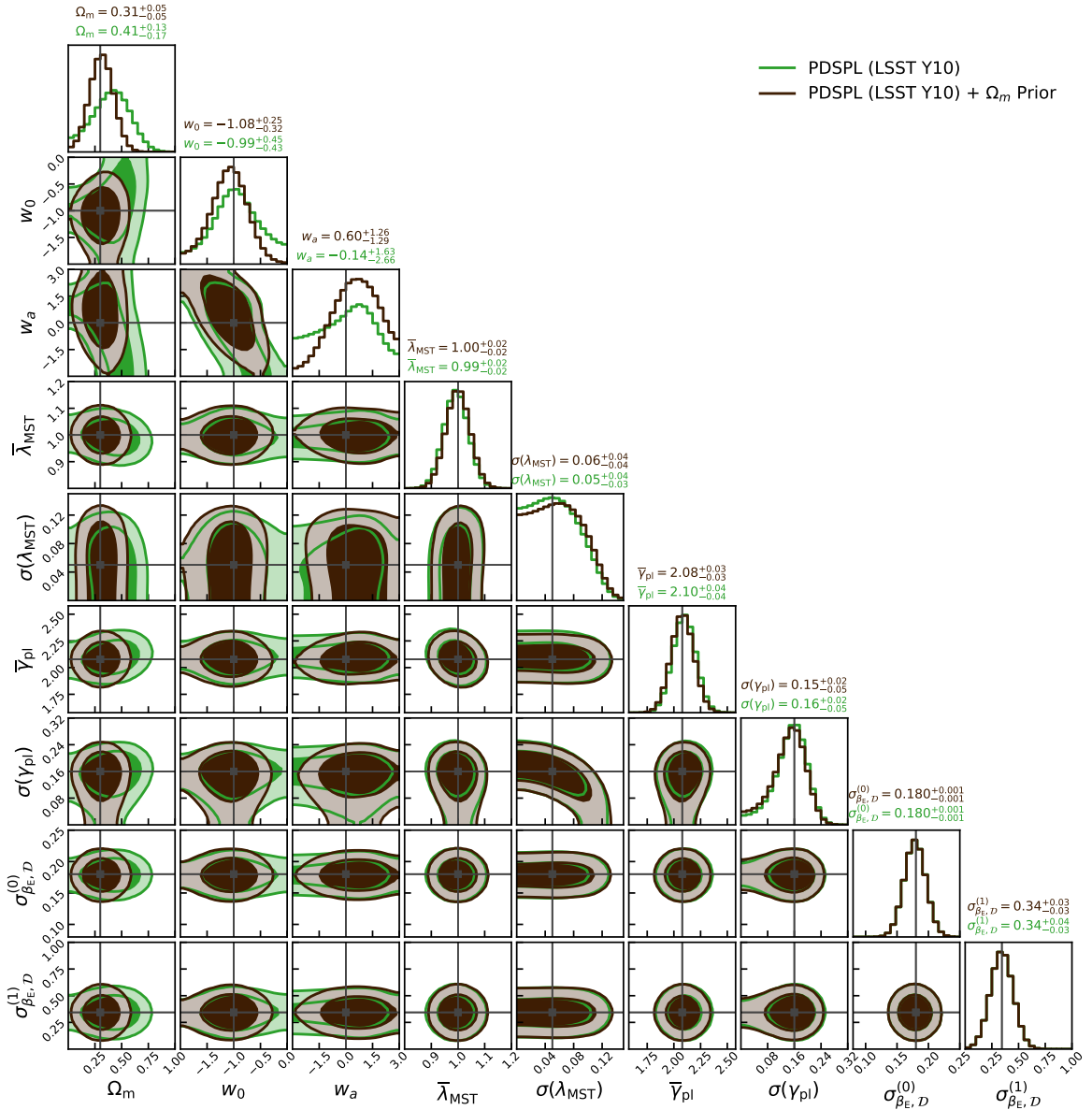


Figure 11. Forecasted posterior distributions for the LSST Y10 PDSPL sample where the intrinsic dissimilarity scatter coefficients ($\sigma_{\beta_{E,D}}^{(0)}$ and $\sigma_{\beta_{E,D}}^{(1)}$) are treated as *free parameters*. Results are shown with (dark brown) and without (green) an external Gaussian prior on Ω_m of $\mathcal{N}(0.3, 0.05)$. The constraints on the dark energy equation of state remain tight, demonstrating the capability of the sample to self-calibrate its own systematic pairing noise.

cosmological constraining power remains approximately the same, validating the robustness of the PDSPL methodology against uncertainties in the pairing noise. However, we note a crucial caveat: these forecasts assume that the functional form of the relationship between the scatter $\sigma_{\beta_{E,D}}$ and the dissimilarity parameter \mathcal{D} is well-described by our chosen linear model (Equation 4.10). In application to real observational data, the exact parametrization of this noise model will not be known *a priori*. Consequently, future analyses will need to explore various functional forms to ensure the self-calibration process remains unbiased.

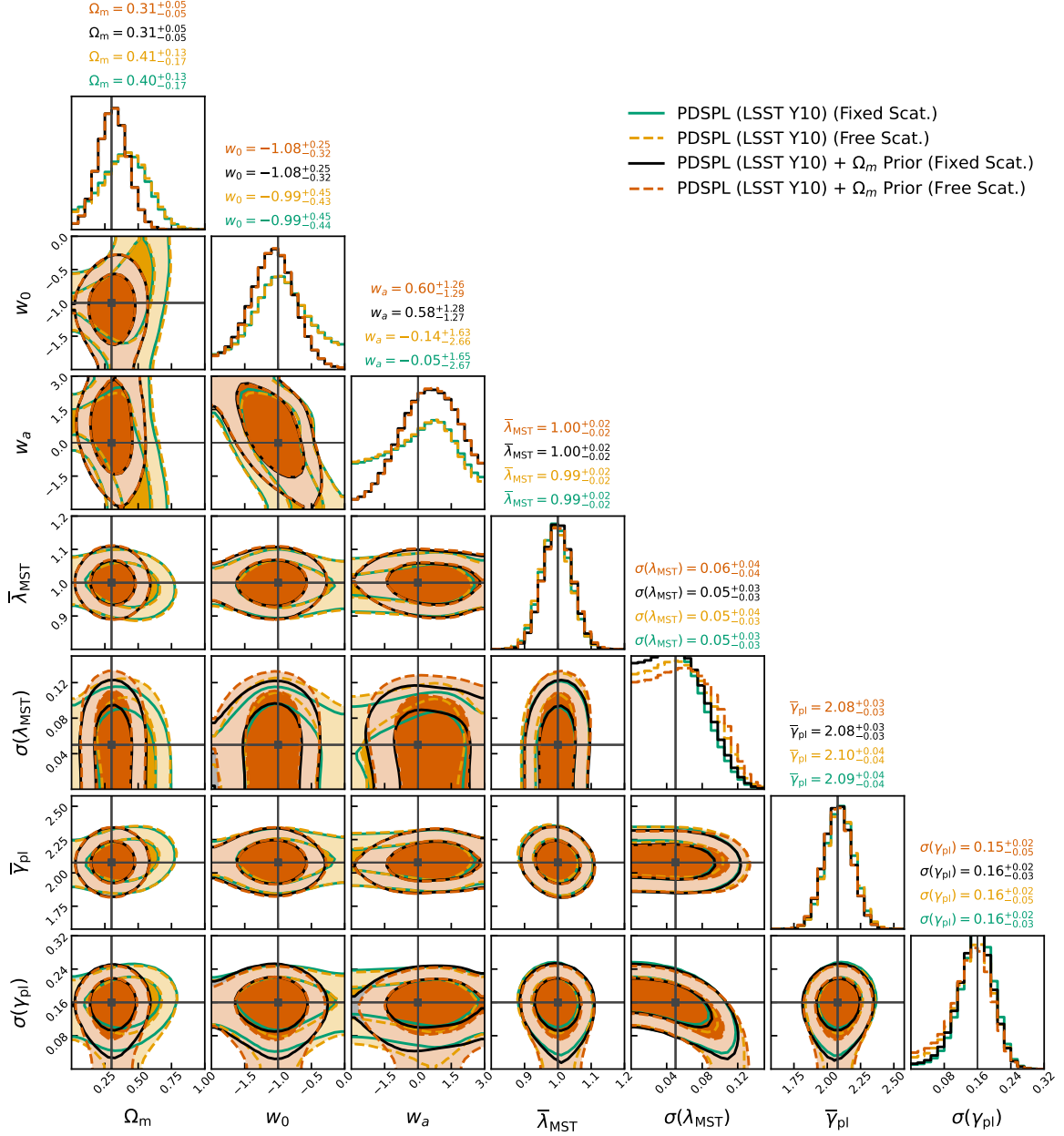


Figure 12. Comparison of the forecasted constraints between the “Fixed Scatter” model (where the dissimilarity relation is perfectly known from simulations; green) and the “Free Scatter” model (where the relation is simultaneously inferred from the data; orange/red) for the LSST Y10 PDSPL sample. Allowing the data to self-calibrate the deflector mismatch scatter results in only a minor degradation of the cosmological parameter constraints.